In-line measurement of the dielectric permittivity of materials during additive manufacturing and 3D data reconstruction

Lukas Fieber[a,*], Syed S Bukhari[a], Yingwei Wu[a], Patrick S Grant[a]

[a]*Department of Materials, University of Oxford, Parks Road, Oxford OX1 3PH, United Kingdom*

Abstract

Additive manufacturing (AM) techniques are used increasingly for the direct fabrication of microwave devices, such as graded index lenses and dielectric resonator antennas, which have spatially-varying dielectric properties (i.e. relative permittivity) that are difficult to manufacture using traditional methods. However, there is no effective method to characterize the spatial distribution of permittivity within the printed component, either during manufacture or once the component is complete. Therefore it is not possible to confirm the extent to which the manufactured spatial distribution of permittivity meets the intended design. We report the integration of a novel split ring resonator (SRR) surface mapping technique directly into an AM process to make non-destructive *in-line* measurements of the local relative dielectric permittivity (ε_r) within 3D objects as they are formed. We then reconstruct these data into 3D dielectric "images" of the printed component. Detailed insights into the dielectric imaging principle, data processing/analysis, as well as limitations and opportunities related to the technique are described. The work aims to accelerate the design-make-test cycle for advanced microwave devices, and suggests the possibility for real-time, *closed-loop* control of dielectric properties during AM.

Keywords: 3D printing, RF devices, In-line quality control, Split ring resonator

*Corresponding author

Email address: lukas.fieber@ccc.ox.ac.uk (Lukas Fieber)

Graphical abstract

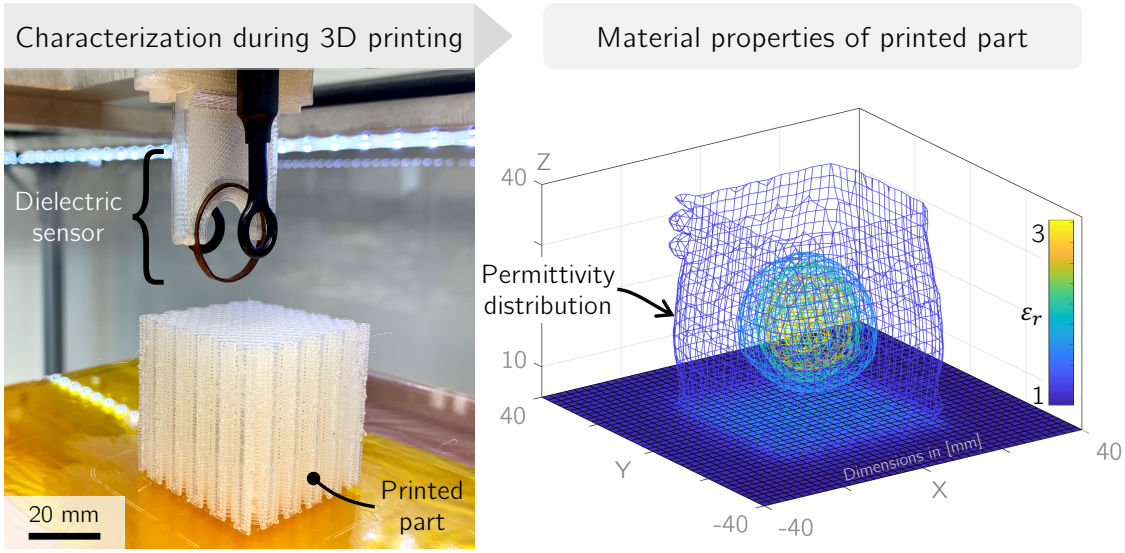

Highlights

- Non-destructive dielectric imaging during additive manufacturing.
- 3D characterization of relative dielectric permittivity within printed devices.
- Integrated, *in-line* quality control technique for AM processes.

1. Introduction

Despite significant progress in the utility, flexibility, speed and accuracy of additive manufacturing (AM) or *3D-printing* technologies, a common, un-met requirement described in review papers and by practitioners is the desire for greater availability of real-time data associated with the evolution of properties within a printed part [1, 2]. For example, in the case of powder bed fusion techniques (such as selective laser melting (SLM) that use metallic powders and a laser to selectively fuse the powder), the *in-situ* real-time distribution of temperature both at fine scale in/near the beam/powder interaction volume, and at the macro-scale over the entire developing three dimensional (3D) object [3–6], is considered useful to understand and ultimately control the tendency for defects such as voids and pores, stresses and distortion, and surface finish [7]. More generally, real-time data could be used to: (a) verify the integrity of parts manufactured by AM (i.e. for quality control (QC) or quality assurance) [8, 9]; and (b) facilitate *reactive manufacturing* and to *close the loop* for dynamic error mitigation by response to live production data [10, 11].

1.1. Characterization of material properties in AM processes

Measurement or metrology systems used in AM processes are generally used to either monitor the manufacturing system parameters (such as bed/nozzle temperatures, deposition speed or rheological properties of extrudates [9, 12, 13]), or characterize the properties of the printed part (e.g. relating to the internal distribution of mechanical material properties [14]). The latter techniques may be further classified as: (a) in-line/in-situ or ex-situ (e.g. integrated strain sensors [14] or post-print X-ray tomography (XRT) analysis [15]), (b) destructive or non-destructive [8, 16], and (c) direct or indirect (e.g. using a proxy such as mechanical impedance for identifying build defects [17]). Different techniques may also be needed for different material classes [18, 19], speed of measurement (e.g. high-speed optical sensing for material jetting [20] or thermography for electron beam melting [10]), and depend on the property of interest, such as strain and temperature [21], tensile properties [22] or surface roughness [23].

In terms of integrating these metrology systems directly into AM processes, challenges include: (a) spatial restrictions – the physical space available to place sensors in the apparatus, especially near the deposition/build zone, is often severely constrained; (b) temporal penalty – acquiring data may be relatively slow so the production rate is undermined; (c) material restrictions – many characterization techniques are restricted to certain material classes e.g. metals [8, 18]; and (d)

data analysis – there is limited understanding of the relationships between the properties that can be measured in the AM environment and the final component properties that are required.

In this paper we investigate the relative dielectric permittivity (ε_r) of just-printed polymers in real-time. The local permittivity and its spatial distribution is of interest because ε_r along with the relative magnetic permeability (μ_r) control the refractive index (n) of the material according to $n = \sqrt{\varepsilon_r \mu_r}$. The spatial control of the refractive index allows the single-operation, direct fabrication (using AM) of novel optical devices for microwave or radio frequency (RF) applications [16, 24, 25]. We note that ε_r may also be a useful proxy measurement of printed properties in other non-metallic AM applications, for example in detecting printing voids. For the examination of metallic materials, other parameters are of interest (since $\varepsilon_r \to \infty$ for metals) and therefore other probes would be needed, beyond the scope of this work. Although there are various well-known characterization techniques for measuring ε_r, their incorporation *in-line* with an AM process has not been reported, and most are unsuitable for the AM environment.

1.2. Additive manufacturing of radio frequency devices

Microwave or RF devices that rely on the controlled spatial variation of electro-magnetic (EM) properties include invisibility cloaks, graded index lenses or dielectric resonator antennas [26–29]. However, engineering progress towards realizing such devices has been slow due to the limitations imposed by conventional manufacturing approaches that are required, for example, to create periodic resonant structures (e.g. metals or ceramics) at sub-wavelength spacing and at large scale [30]. Because AM forms parts incrementally, *layer-by-layer*, it provides an opportunity to overcome these conventional limitations by depositing/building different materials at different locations and with sufficient, sub-GHz wavelength spatial resolution. For example, fused filament fabrication (FFF) has been used to print selectively in different places a variety of particulate composite materials, each with a different ε_r to form a graded index lens [16]. Other approaches include inkjet printing (IJP) or assembly of heterogeneous metal-polymer composites [31]. Moreover, as we show in this work the layer-by-layer nature of AM can be exploited to allow measurement of each layer, or each track within a layer, *in-line* and throughout build [11, 14], and then reconstructing these data in 3D.

1.3. Electro-magnetic characterization techniques

Techniques for characterizing the EM properties of dielectric materials and devices have been reviewed frequently [32–34] and may generally be classified as: (a) resonant or non-resonant (e.g. split post dielectric resonator (SPDR) [35] or parallel plate capacitors [36]), (b) free-space or guided (e.g. scattering patterns [37] or waveguide measurements [38]), and (c) reflection or transmission (e.g. a 1-port coaxial probes [39] or 2-port striplines [40]). Other attributes of EM characterization techniques include: (a) the sampled frequency range (e.g. narrow- or broad-band), (b) the required resolution, (c) sample preparation requirements (e.g. surface roughness/finish or sample dimensions), (d) the nature or type of the material (i.e. solids, gels or liquids), (e) destructive or non-destructive (i.e. requiring physical modification/contact with the sampled part), and (f) cost.

Only very few of the available EM characterization techniques may be considered suitable for easy, direct integration into AM processes. Common limitations include: (a) danger of cross-contamination and damaging of the printed part through probe contact; (b) the need for controlled ambient EM environments; and (c) stringent requirements on surface roughness and other geometric tolerances. Here we select a novel approach to measuring the spatial ε_r distribution of a solid surface based on a two dimensional (2D) mapping technique using a split ring resonator (SRR) [19]. The SRR technique may be classified as resonant, free-space and transmission-based and does not intrinsically suffer from the limitations (a) to (c) above. The SRR technique is a narrow-band resonant method, and if the printed material is expected to show permittivity as a strong function of frequency, other resonant ring sizes (frequencies) could be employed.

1.4. Current work

In this paper, we show proof-of-concept (PoC) for a non-destructive, non-contact dielectric imaging technique, *in-line* with an AM process to characterize the spatial distribution of the relative dielectric permittivity (ε_r) within a printed part. An in-house developed 2D dielectric imaging technique based on a split ring resonator (SRR) [19] is extended to operate without physical contact (non-destructive) and is integrated into a bespoke hybrid-AM machine. 2D dielectric "images" of each printed layer are recorded and processed to reconstruct the relative dielectric permittivity (ε_r) distribution in 3D. We suggest how this approach may accelerate the RF device design cycle, facilitate the fabrication of RF devices with complex, useful wave-material interactions, and

form the basis for future work on *closed-loop*, feedback-controlled AM of parts with heterogeneous dielectric properties.

2. Materials & methods

2.1. Hybrid additive manufacturing

A bespoke, hybrid-AM machine was designed, built and commissioned allowing for up to 9 complementary AM and *in-line* characterization techniques to be automated into a single, numerical control (NC) operation [41]. The machine is shown in Figure 1a and key features are labelled (i) to (v) as follows: (i) an in-house built split ring resonator (SRR) module (see Appendix A.1 for a sub-assembly drawing) connected to (ii) a vector network analyzer (VNA) (ZNB20, Rohde Schwarz, Germany) and (iii) a computer running custom control software. Multiple (iv) fabrication modules including fused filament fabrication (FFF) extrusion heads were installed for the purpose of fabricating multi-material devices on (v) a temperature controlled build platform. The primary parameters describing the geometry and operation of the split ring resonator (SRR) probe are shown in Figure 1b and c.

Custom printing software was developed to allow for the simultaneous control of the hybrid-AM machine and the VNA, i.e. to send, receive and log commands or queries to/from the various microelectronic and measurement sub-systems. The software provided a platform to interact with all system components and also allowed for: (a) debugging of control commands and queries (i.e. the `g-Code`), (b) manual machine control (e.g. for calibration purposes), (c) analysis and visualization of production/characterization data and (d) identification of unusual parameters in case of faulty system components. A screenshot of the printing host graphical user interface (GUI) is shown in Appendix A.2.

3D demonstrator components for AM were designed in computer aided design (CAD) software (SolidWorks 2017) before being exported as surface geometries (STL files). Open source slicing software (Slic3r v1.3.0) was used to generate a *layer-by-layer*, machine interpretable code (`g-Code`), which was thereafter automatically modified by the printing software (post-slicing modifications) to reflect calibration values and to include the additional tool-paths necessary to automatically characterize (using the SRR probe) the component as it formed. AM parts were fabricated using a FFF hot-end (TitanAero from E3D, UK with a $\varnothing = 0.6\,\text{mm}$ brass nozzle) using commercially

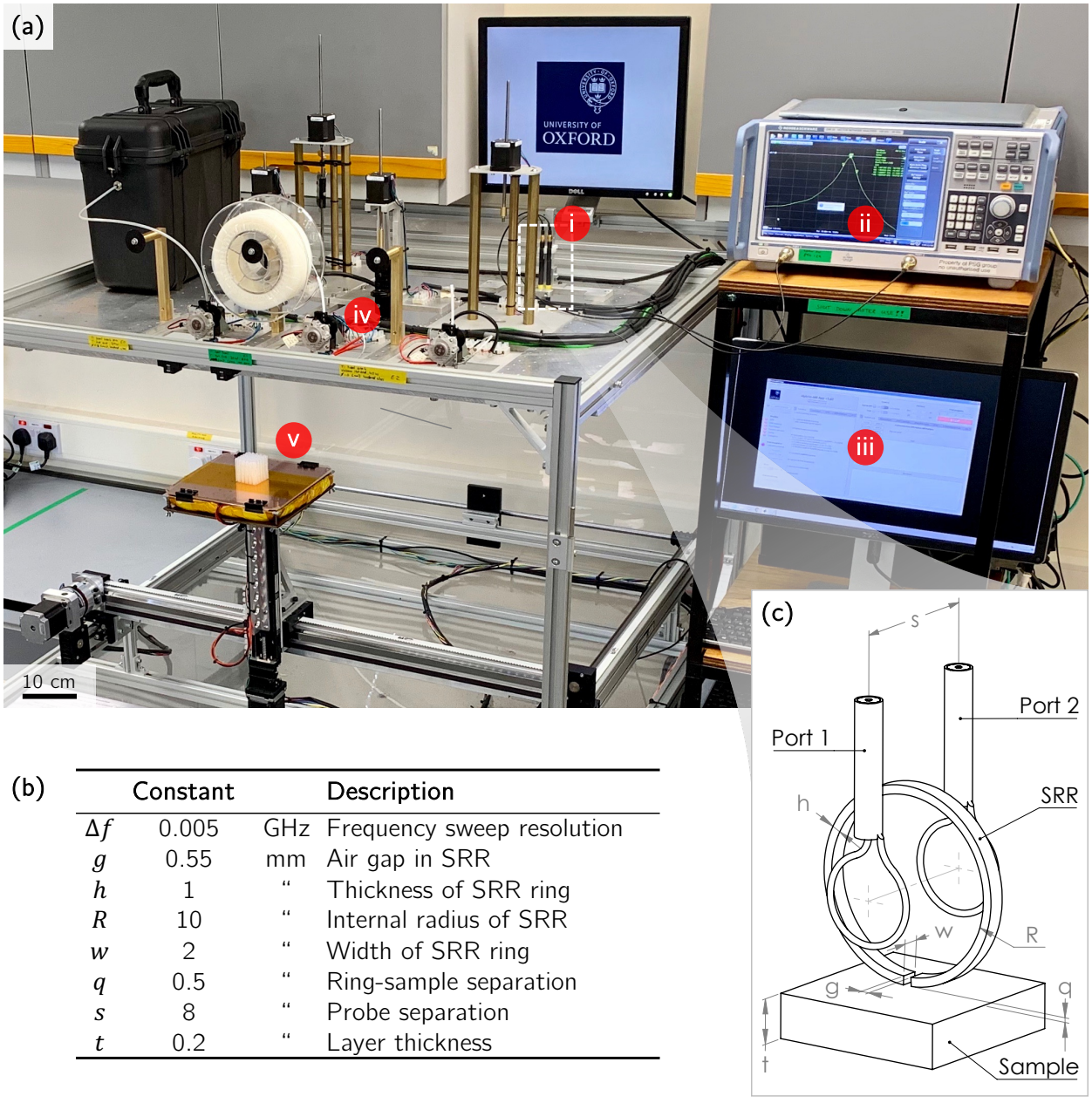

(b)

	Constant		Description
Δf	0.005	GHz	Frequency sweep resolution
g	0.55	mm	Air gap in SRR
h	1	"	Thickness of SRR ring
R	10	"	Internal radius of SRR
w	2	"	Width of SRR ring
q	0.5	"	Ring-sample separation
s	8	"	Probe separation
t	0.2	"	Layer thickness

Figure 1: (a) A photograph of the hybrid-AM machine showing: (i) the SRR probe connected to (ii) a VNA, (iii) a control computer, (iv) functional modules including FFF hot-ends and (v) the temperature controlled build platform. (b-c) The primary geometric and operating parameters used for the SRR probe.

available polymer filament (Natural polylactic acid (PLA) from Spoolworks, UK) with $\varepsilon_r = 2.71 \pm 0.06$ at print speeds of $30\,\mathrm{mm\,s^{-1}}$, and nozzle/build-platform temperatures of 192 °C and 40 °C respectively. Consistent with previous work, the ε_r of printed PLA was assumed to be independent of temperature over the range used in this study and at frequencies in the low GHz spectrum [42].

2.2. Electro-magnetic characterization techniques

Figure 2 schematically illustrates the operating principle of the SRR probe: (a) two magnetic field ($\vec{\mathbf{H}}$ field) probes (RF-R 50-1, Langer EMV, Germany) were placed at equal distance from a single Cu split ring resonator (SRR), at a separation distance $s = 8\,\mathrm{mm}$ and connected to a VNA using flexible coaxial cables (1 m SMA-SMA, Langer EMV, Germany); (b) the probes induced an electric field ($\vec{\mathbf{E}}$ field) across the SRR and its fundamental resonant frequency (f_0) in free space was evaluated by searching for the local maximum in transmission (S_{21}) over a frequency sweep $f \in [1.5, 1.9]$ GHz at specified resolution $\Delta f < 1\,\mathrm{MHz}$; (c) f_0 was then influenced by the presence of an introduced material with $\varepsilon_r > 1$ in the fringing $\vec{\mathbf{E}}$ field across the SRR air gap that resulted in; (d) a shift in f_0 that was recorded by the VNA. Finally, (e) contributions related to the sample ε_r were isolated from other factors and, (f) by post-processing of the SRR resonant frequency map $f_0(\vec{\mathbf{x}})$; a (g) spatial permittivity map $\varepsilon_r(\vec{\mathbf{x}})$ was obtained.

For validation, the intrinsic relative dielectric permittivity of the printed PLA filament was also measured using conventional Nicolson-Ross-Weir (NRW) waveguide methods according to [43]. Reflection and transmission data was collected from a 2 mm thick sample (printed using FFF, 100 % infill) which was placed in a rectangular waveguide (No. 18094-SF40, Flann, UK) operating in mode $TE_{1,0}$ over the frequency range 12 to 18 GHz.

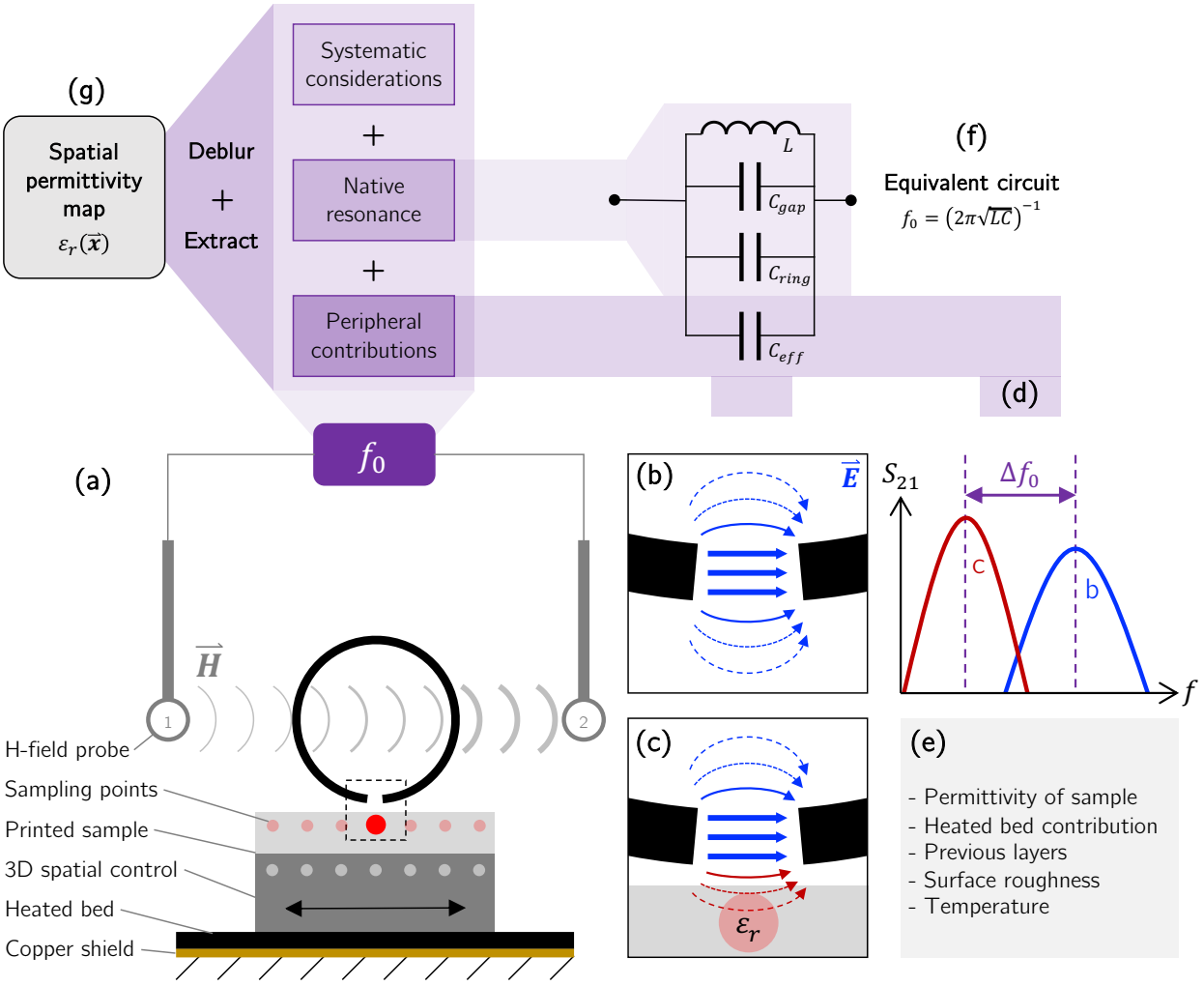

Figure 2: A schematic illustration of the SRR operating principle depicting: (a) the SRR, (b) the $\vec{\mathbf{E}}$ field in free space and (c) under the influence of a material $\varepsilon_r > 1$, (d) the resulting shift in resonant frequency Δf_0, (e) a sub-set of parameters influencing the resonant frequency, (f) an equivalent circuit for interpreting the frequency shift, and (g) the resulting spatial permittivity map.

2.3. Simulation

Full-wave EM simulations of the SRR system were conducted in Comsol Multiphysics. The geometry of the SRR probe was derived from a CAD model with dimensions comparable with the experimental set-up shown in Figure 1. The $\vec{\mathbf{H}}$ field probes were modelled as simplified, planar (2D) rings of $\varnothing 10\,\mathrm{mm}$, equi-distant from the SRR with a probe-probe separation distance $s = 8\,\mathrm{mm}$ and lumped port impedances of $50\,\Omega$ to model the coaxial, SMA connectors used. The SRR was modelled as an ideal, perfect electric conductor in free space (without the SRR holder, see Appendix A.3), and all surfaces were considered to be perfectly flat. The quasi-infinite, spherical finite elements model (FEM) boundary was defined as a perfectly matched layer (PML). The FEM mesh size was limited to $< \lambda/5$, and areas of interest (e.g. between the SRR gap and sample) were refined by a factor of 4 to provide mesh-independent solutions. The SRR resonant frequency f_0 was determined numerically using a coordinate search $f \in [1.5, 3]$ GHz, maximizing for the port transmission parameter S_{21}, i.e. f_0 at $max(S_{21})$, to an optimality tolerance of $S_{21,dB} < 0.005$ (approximately equal to the nearest 1 MHz to match the VNA sweep resolution used in experiments). Appendix A.3 shows that the transmittance response $S_{21}(f)$ of the simplified, simulated SRR probe matched the experimental data closely, with experimental and simulated values of f_0 matching to within $\pm 2\,\mathrm{MHz}$.

3. Results and discussion

The key steps involved in measuring the spatial distribution of relative dielectric permittivity (ε_r) within printed parts were: (i) the resonant frequency (f_0) of the split ring resonator (SRR) was measured (i.e. sampled at discrete locations *layer-by-layer* and *in-line* with AM), (ii) a deblurring post-processing step was applied to enhance the spatial resolution, and finally (iii) an *extraction* model was applied to obtain a 3D, spatial $\varepsilon_r(\vec{\mathbf{x}})$ map of the printed object. Figure 3 schematically shows steps (i) to (iii) above, alongside corresponding 3D contour maps of experimental data showing the resonant frequency for: (a) an empty build platform, termed $f_{ref}(\vec{\mathbf{x}})$, (b) an arbitrary 3D shape (PLA, 100 % infill), termed $f_0(\vec{\mathbf{x}})$, and (c) the same shape after deblurring, termed $f_{0d}(\vec{\mathbf{x}})$. Note that the 3D data presented in Figure 3 is a reconstruction of successive X-Y imaging planes incrementing in the Z direction.

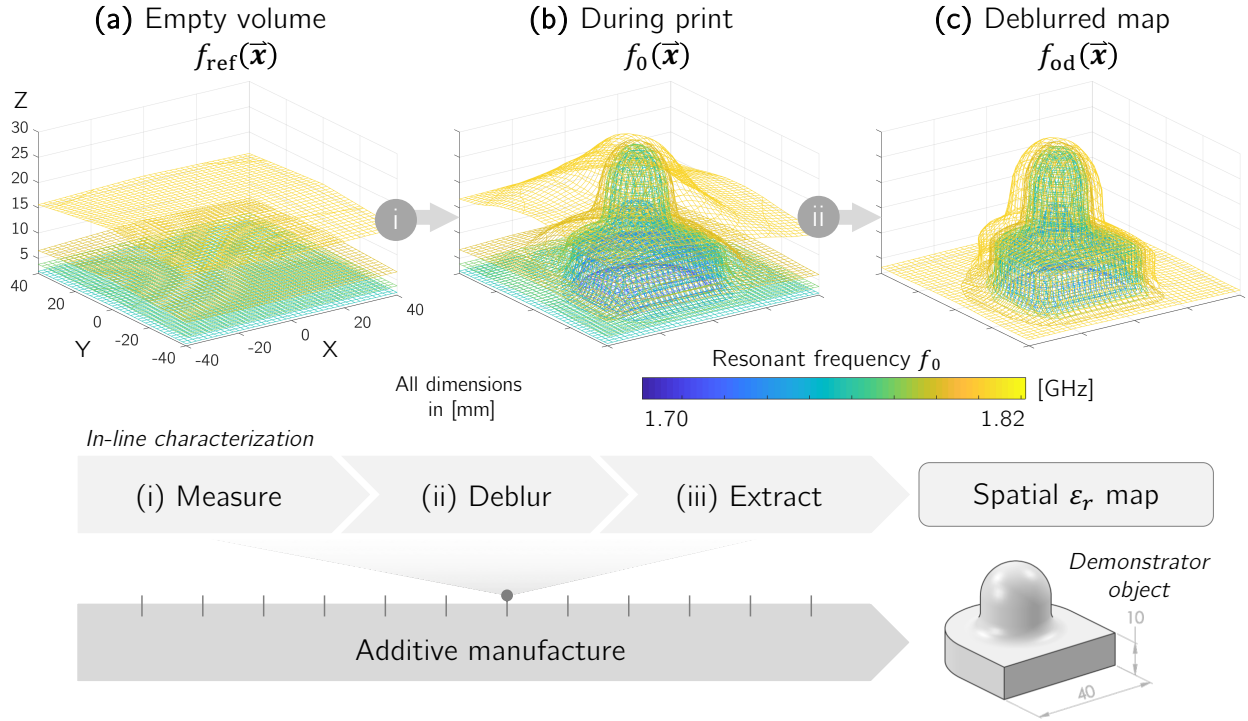

Figure 3: A schematic flowchart of the steps (i-iii) involved in the non-destructive, *in-line* dielectric characterization technique and 3D contour maps of resonant frequency (f_0) data for: (a) an empty build $f_{ref}(\vec{\mathbf{x}})$ (free space), (b) during manufacture of the demonstrator object, showing the permittivity contribution of the printed part $f_0(\vec{\mathbf{x}})$, and (c) the sample data after deblurring $f_{0d}(\vec{\mathbf{x}})$.

3.1. Measurement – In-line sampled frequency map

Figure 4a shows a photograph of the SRR probe in relation to a printed demonstrator during the later stages of fabrication. Figure 4b, c and d show *raw*, unprocessed experimental resonant frequency data from *in-line* measurement: (b_1) is a Y-Z plane in free space showing only the (weak) permittivity influence of the build platform, i.e. $f_{ref}(\vec{\mathbf{x}})$, and ($b_2$) is the same Y-Z plane but now with the additional contribution/influence of the printed object, i.e. $f_0(\vec{\mathbf{x}})$; (c) is a X-Y plane of $f_0(\vec{\mathbf{x}})$, and (d) is the reconstructed data in 3D showing the location of the preceding 2D sections shown in (b) and (c). The local resonant frequency was influenced by: (a) a contribution from the just-printed part (referred to as *peripheral* contributions), (b) the native or *intrinsic* f_0 of the SRR probe (described in Appendix B), and (c) other contributions from the overall ambient environment/system (described in Appendix C).

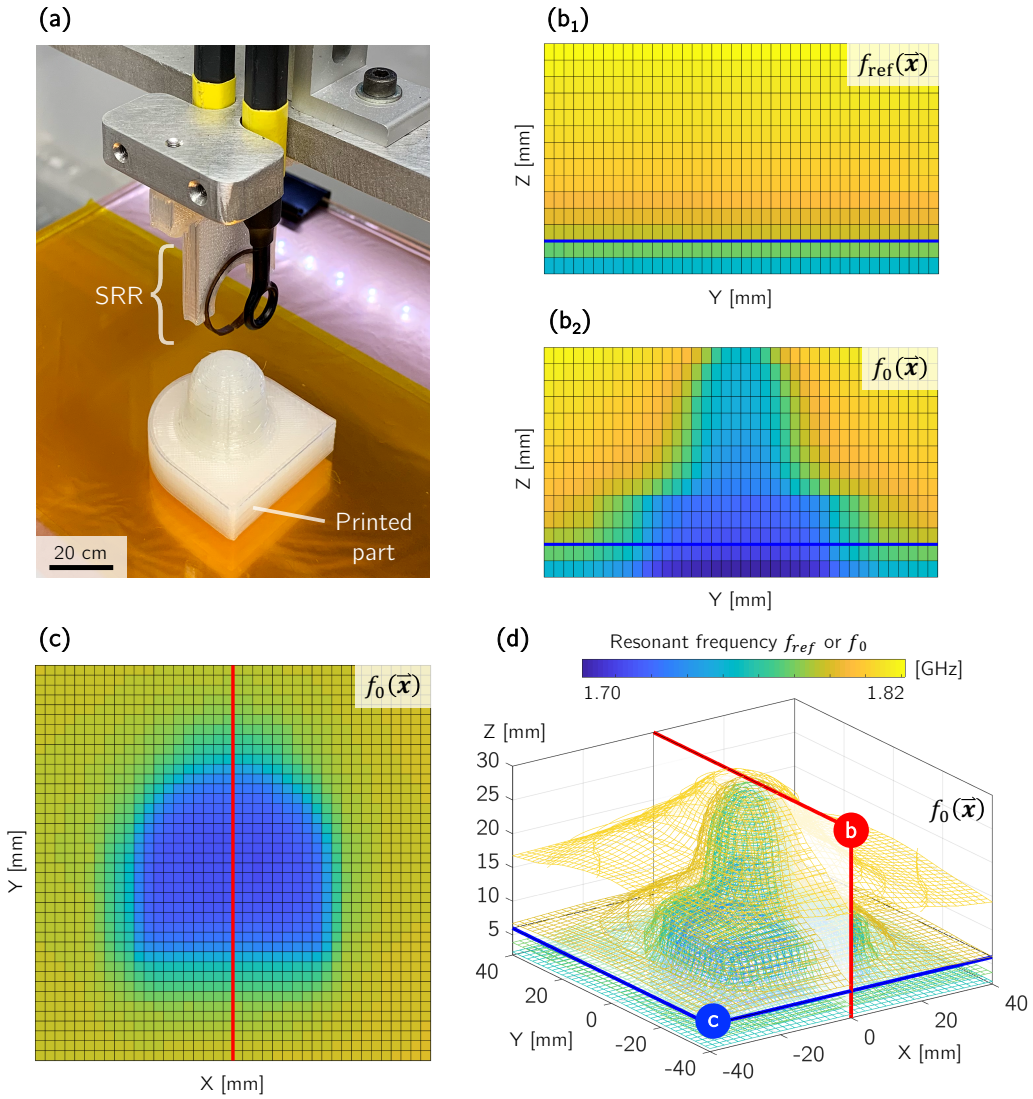

Figure 4: (a) A photograph of the SRR probe during operation and (b-d) *raw*, unprocessed experimental resonant frequency data from *in-line* measurements: (b_1) a Y-Z plane showing only the contribution of the build platform, (b_2) the same Y-Z plane with additional contributions from the printed part, (c) a X-Y plane of the frequency data in (b_2) and (d) a 3D contour map showing the location of the cross-sections in (b) and (c).

3.1.1. Peripheral contributions

Permittivity dependence. While both the intrinsic f_0 of the SRR, and any ambient environment/systematic contributions were considered to remain constant throughout sampling, the shift in f_0 with position, i.e. $f_0(\vec{\mathbf{x}})$ in Figure 4, was attributed to a change in the local environment (i.e. the *peripheral* conditions) sampled by the SRR. This arose due to distortion of the fringing fields associated with the induced $\vec{\mathbf{E}}$ field across the SRR gap (schematically illustrated in Figure 2c) when close to materials with a permittivity different from air. This may be interpreted as a change in total ring capacitance (contribution of C_{eff} in Figure 2f), and leads to the measured shift in f_0. By simulating the SRR close to an ideal, quasi-infinite material with user-specified, varying EM properties ($\varepsilon_r \in [1, 50]$), a logarithmic relationship between f_0 and ε_r was established:

$$\frac{\partial f_0}{\partial \varepsilon_r} \propto \frac{M_e}{\varepsilon_r} \tag{1}$$

where M_e was a best-fit coefficient dependent on the SRR geometry. Data to support Equation (1) is shown subsequently in Figure 8b. The non-linearity of Equation (1) shows that with increasing permittivity, the absolute sensitivity of the technique decreases.

Probe-sample separation distance. Both simulation and experiment showed the SRR resonant frequency was sensitive to the probe-sample separation distance (q). Equation (2) below expresses the relationship between f_0 and q that was established by simulating a quasi-infinite sample (i.e. all sample dimensions exceeding the sampling volume size) with $\varepsilon_r \in [1, 10]$ for $q > 0.05\,\text{mm}$:

$$\frac{\partial f_0}{\partial q} \propto \frac{\exp(M_q \times q^n)}{q^{1-n}} \tag{2}$$

where $n = 0.1$ and $M_q < 0$ were best-fit coefficients. Data to support Equation (2) is again shown subsequently in Figure 8c. In other words, the closer the SRR was to the sample (i.e. $q \to 0$), the more noticable (larger Δf_0) the contribution of the sample to the frequency shift (i.e. a stronger *signal*). However in practice, when the SRR was too close to the printed part ($q < 0.2\,\text{mm}$), inevitable surface printing imperfections (e.g. stringing, blobs and zits) came into physical contact with the SRR, invalidating readings by possible deformation of the SRR. Appendix B provides an indication of the sensitivity of f_0 to changes in ring geometry. Therefore, a probe-sample separation distance $q \in [0.5, 1]$mm was identified as a reasonable compromise between attaining sufficient

signal strength (dynamic range) while preventing occasional surface undulations from touching the SRR. The probe-sample separation distance used for all data shown here was $q = 0.5\,\text{mm}$.

Surface roughness. Given the comments above, the surface roughness of printed parts using optimized printing parameters was evaluated using whitelight confocal microscopy (NanoFocus μSurf) as $R_a = 0.7\,\mu\text{m}$ parallel to the print direction and $R_a = 6.4\,\mu\text{m}$ perpendicular to the print direction. The effect of typical surface roughness on the SRR signal was therefore considered to be negligible due to the large difference in roughness length scale when compared with the probe-sample separation distance (q) $\sim 0.5\,\text{mm}$.

Automatic calibration. Let $f_{0,air}$ be the intrinsic resonant frequency of the SRR in free space and $f_{0,bed}$ the resonant frequency of the SRR at a separation distance q between the SRR and the build platform (see Figure 1c for a definition of q). Simulations indicated that for $q = 0.5\,\text{mm}$, the shift in f_0 compared to the native $f_{0,air}$ of the SRR in free space (i.e. the dynamic range $DR_{bed} = f_{0,air} - f_{0,bed}$) should equal $DR_{bed} = 140\,\text{MHz}$. In order to accurately and repeatably reach the chosen probe-sample separation distance of 0.5 mm in practice, the build platform approached the SRR in small increments (Z-steps of $> 3.4\,\mu\text{m}$) while monitoring the shift in f_0. Once $DR = 140\,\text{MHz}$ was reached, with knowledge of $f_{0,air}$ and $f_{0,bed}$, the best-fit coefficients M_e and M_q in Equations (1) and (2) could be obtained. Experiments showed that the desired probe-sample separation distance could be achieved repeatedly to within $\pm 5\,\mu\text{m}$. The calibration process is shown schematically in Appendix A.4.

Sampling volume. The signal (f_0) recorded at point $\vec{\mathbf{x}}$ was not only influenced by the dielectric properties of the *desired sampling point* directly below the ring split, but also by the aggregate contribution of a large, weighted *sampling volume* that influenced the $\vec{\mathbf{E}}$ field. Figure 5a shows the simulated SRR sampling volume, which was approximately hemi-spherical. It is this sampling volume effect that explains the *blurring* in the f_0 maps at the object edges in Figure 4. The sampling volume in Figure 5a was modelled as a distribution directly proportional to the simulated magnitude of the $\vec{\mathbf{E}}$ field within a dielectric material (i.e. a 3D, point spread function (PSF) $\propto |\vec{\mathbf{E}}|$). The shape/dispersion and in particular the *penetration depth* (in the vertical Z-axis) of the sampling volume was a function of the material ε_r (a higher ε_r resulted in a more shallow sampling volume). The sampling volume associated with a SRR operating at wavelength $\lambda \sim 15\,\text{cm}$ (2 GHz in free space) was approximately $\lambda/11$ (i.e. ranging from -7 to 7 mm in the PSF in Figure 5a). This provided a good estimate of the default spatial resolution of the characterization technique, i.e. the minimum achievable distance between two fully decoupled measurements.

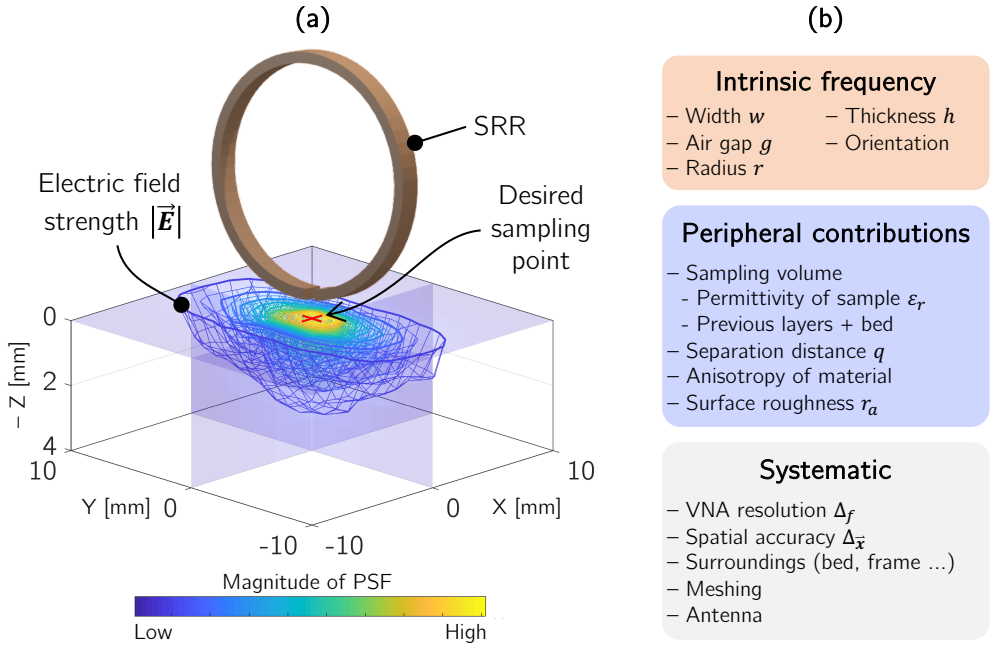

Figure 5: (a) A 3D contour-plot of simulation data showing the sampling volume (linearly proportional to the magnitude of the induced $\vec{\mathbf{E}}$ field within the sample, i.e. point spread function (PSF) $\propto |\vec{\mathbf{E}}|$) for an ideal, quasi-infinite material with $\varepsilon_r = 3$, and (b) an overview of the primary factors influencing the resonant frequency (f_0) of a SRR.

3.2. Deblurring – Improving spatial resolution

To account for the blurring and to enhance the spatial resolution of the resonant frequency map $f_0(\vec{\mathbf{x}})$ (i.e. step ii in Figure 3), a post-processing method referred to as *deblurring* was developed and entailed: (a) the expansion and enhancement of $f_0(\vec{\mathbf{x}})$ in space, (b) 3D deconvolution thereof using a single, approximated point spread function related to the shape of the sampling volume shown previously, and (c) contraction of the expanded, deconvoluted map to generate a refined frequency map $f_{0d}(\vec{\mathbf{x}})$ matching the original size of $f_0(\vec{\mathbf{x}})$.

To enhance the sampling resolution despite the relatively large PSF (comparable in size with the object features), it was imperative to *taper* the edges of the data set. This was necessary to minimize the ringing effect induced by deconvolution [44]. To preserve information near the edges of $f_0(\vec{\mathbf{x}})$, the data set was expanded/extrapolated before being tapered. Figure 6 shows an expanded data-set (prior to deconvolution) and highlights how data from an empty volume scan (f_{ref} in Figure 3), alongside $f_{0,air}$ and $f_{0,bed}$ (from the automatic calibration process described in Section 3.1), was used to extrapolate the data.

The PSF from Figure 5a was used to deconvolute the newly expanded, tapered frequency map from Figure 6 in a single iteration. It should be noted that the sampling volume in Figure 5a was truncated to consider only the contribution of already printed layers (i.e. the materials beneath the SRR and the surface of the sample at the time of measurement) and to ignore the contribution of air above the surface of the sample, resulting in an asymmetric PSF (but more computationally efficient) where the PSF= 0 for all locations where $Z > 0$. Figure 7a shows a plot of f_0 as a function of X for the X-Z section shown in Figure 7b, indicating the effect of deconvolution in the resulting maps for $f_{0,d}(\vec{\mathbf{x}})$. With reference to the labels in Figure 7, deconvolution led to: (i) a reduction in the range of resonant frequency within a single material, and (ii) much improved dielectric isolation of the build-platform contribution.

To quantify the improvement in spatial resolution due to *deblurring*, consider the SRR with resonant frequency $f_{0,air}$ in free space, and with $f_{0,s}$ when in proximity to a large sample ($\varepsilon_r > 1$ and all dimensions exceeding the size of the PSF). The dynamic range (DR) for this system is defined as $DR = |f_{0,air} - f_{0,s}|$. We define the spatial resolution of the SRR technique as the step (in $\vec{\mathbf{x}}$) required to resolve a 10 % shift in f_0 when transitioning across a physically sharp interface between the sample and air, i.e. $\Delta f_0 = 0.1 \times DR$. Using this definition, for a sample with $\varepsilon_r = 10$,

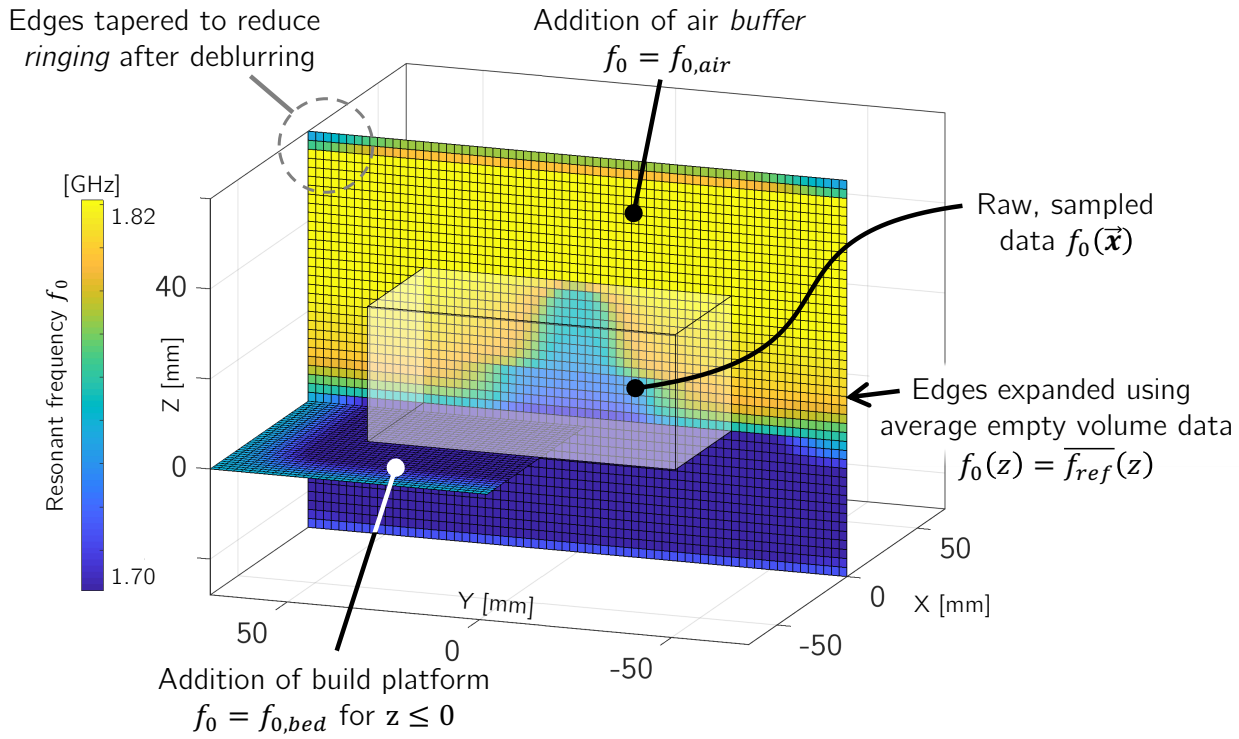

Figure 6: The expansion and enhancement of 3D experimental data ($f_0(\vec{\mathbf{x}})$) with tapered edges, addition of air and build platform buffers alongside extrapolation of edges using reference data for an empty scan (f_{ref}).

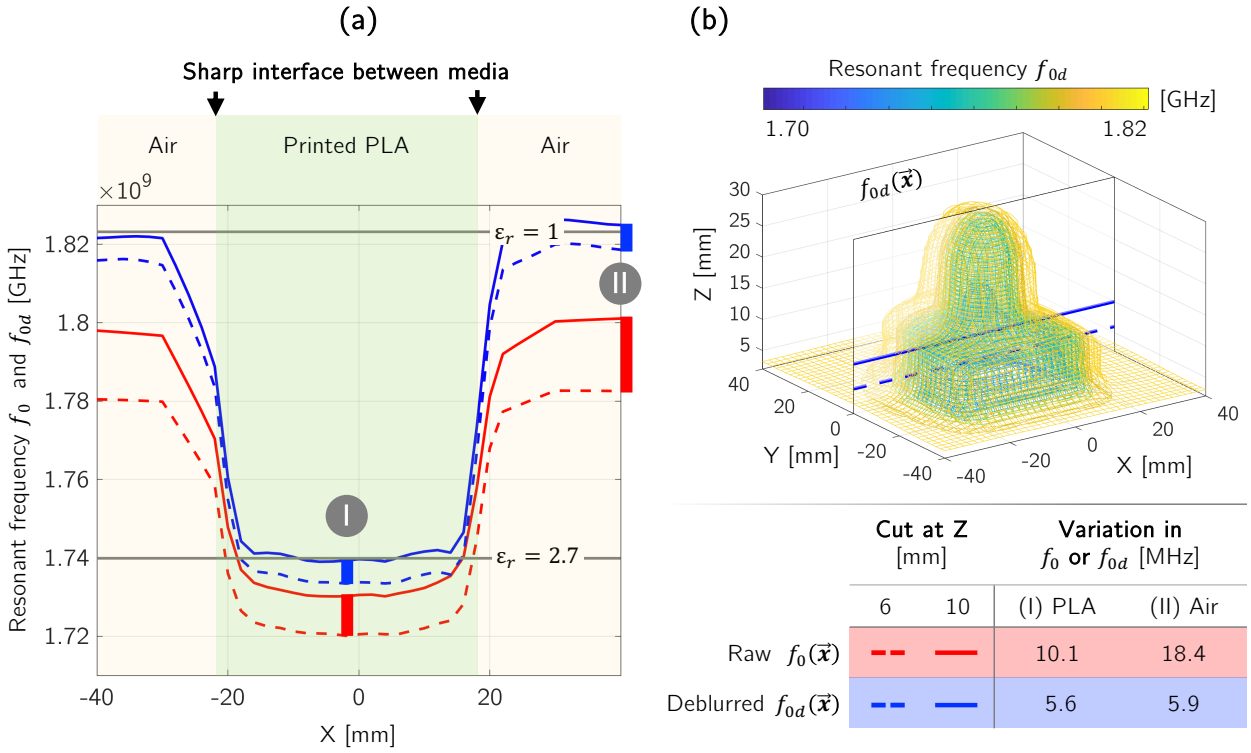

Figure 7: Deblurring of experimental data showing: (a) various sections of data (raw/unprocessed f_0 data and deblurred f_{0d} data) at different heights and (b) the location of the X-Z sections taken from the 3D reconstruction.

deblurring achieved a spatial resolution improvement of at least $\times 1.6$, from $\pm 6.4\,\text{mm}$ or $\lambda/11$ to $\pm 4.0\,\text{mm}$ or $\lambda/18$ where λ is the resonance wavelength of the SRR. Figure A.5 shows supporting simulation data to assess the spatial resolution limit of an ideal SRR. It should be noted that the spatial resolution was dependent on ε_r because the simplified PSF function used in deblurring was itself related to the fringing $\vec{\mathbf{E}}$ fields of the SRR, which were again dependent on ε_r.

3.3. Extraction – Interpreting the resonant frequency

A model to translate the frequency maps to relative dielectric permittivity (ε_r) maps (i.e. step iii in Figure 3), while taking into account the SRR probe-sample separation distance q, was derived from Equations (1) and (2). The *extraction model* is expressed in Equations (3) and (4) below and is shown graphically in Figure 8:

$$f_{0d} = f_{0,air} - DR \times \exp\left(M_q \times q^{0.1}\right) \tag{3}$$

$$DR = M_e \ln(\varepsilon_r) \tag{4}$$

where $f_{0,air}$ is the intrinsic resonant frequency of the SRR in free space (see Appendix B), DR is the dynamic range as a function of relative dielectric permittivity (ε_r), q is the sample-SRR separation distance, and M_q and M_e are sensitivity factors related to q and ε_r respectively. Combining Equations (3) and (4) yields:

$$\ln(\varepsilon_r) = \frac{f_{0,air} - f_{0d}}{M_e \times \exp\left(M_q \times q^{0.1}\right)} \tag{5}$$

The *extraction model* allowed for an extraction curve (i.e. $\varepsilon_r(f_0)$ at constant q, see label i in Figure 8a) to be deduced for any specified experimental set-up. The dynamic range DR in Equation (4) is a logarithmic best-fit over a sample permittivity range $\varepsilon_r \in [1, 50]$ and is shown for $q \in [0.5, 2]$mm in Figure 8b. The relationship between resonant frequency f_0 and probe-sample separation distance q is shown in Figure 8c.

Figure 9 shows a 3D spatial $\varepsilon_r(\vec{\mathbf{x}})$ map of a printed demonstrator with deliberately varying local fill density to provide a range of local ε_r, between air ($\varepsilon_{r,air} = 1$) and printed PLA ($\varepsilon_{r,PLA} = 2.71$). The demonstrator, shown in Figure 9a and b, comprised a $\varnothing$20 mm sphere (100 % infill) centered within a 40 mm cube (25 % infill). The dimensions of printed features could be deduced from the ε_r map in Figure 9c and d to an accuracy of ± 2 mm. The average ε_r measured for the 25 % dense box around the sphere was 1.46, in excellent agreement with a Wiener's formula based estimate of 1.43 [45], and suggested a typical accuracy of approximately 5 % for materials in this permittivity range. Although the work in this paper has used PLA only, the FFF process benefits from a very

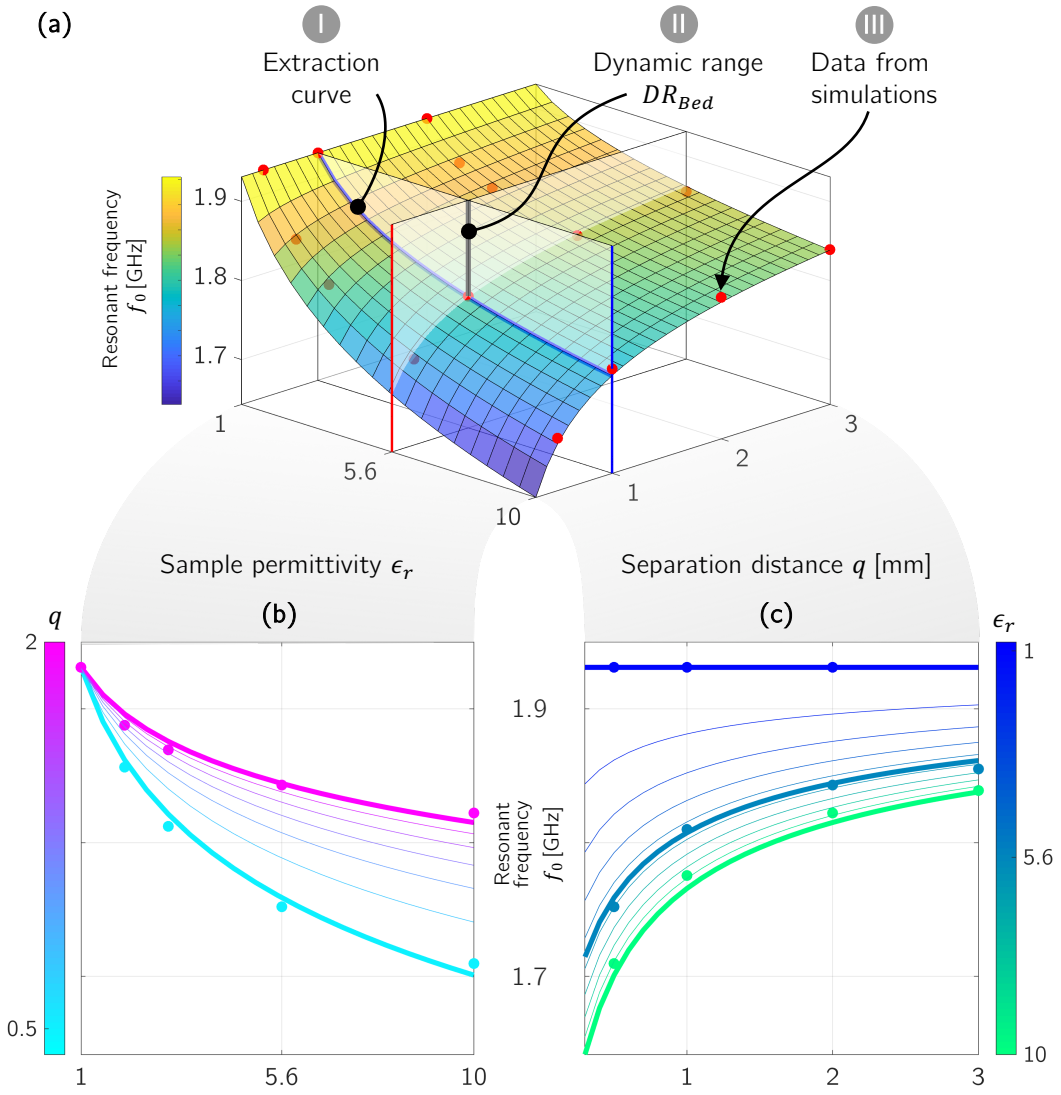

Figure 8: (a) A 3D surface plot showing the *extraction function* for converting SRR resonant frequency f_{0d} into permittivity ε_r while accounting for SRR probe-sample separation distance q. An indicative (I) extraction curve at $q = 1\,\text{mm}$ is highlighted, alongside (II) the dynamic range DR_{Bed} associated to the build platform and (III) data points from simulations. Cross-sections highlighting contours at (b) $q = [0.5, 2]\text{mm}$ and (c) $\varepsilon_r = [1, 5.6, 10]$ are also shown.

wide and increasing range of commercial polymer and polymer-composite filament materials, all of which could be investigated in their printed form using the *in-line* SRR probe approach.

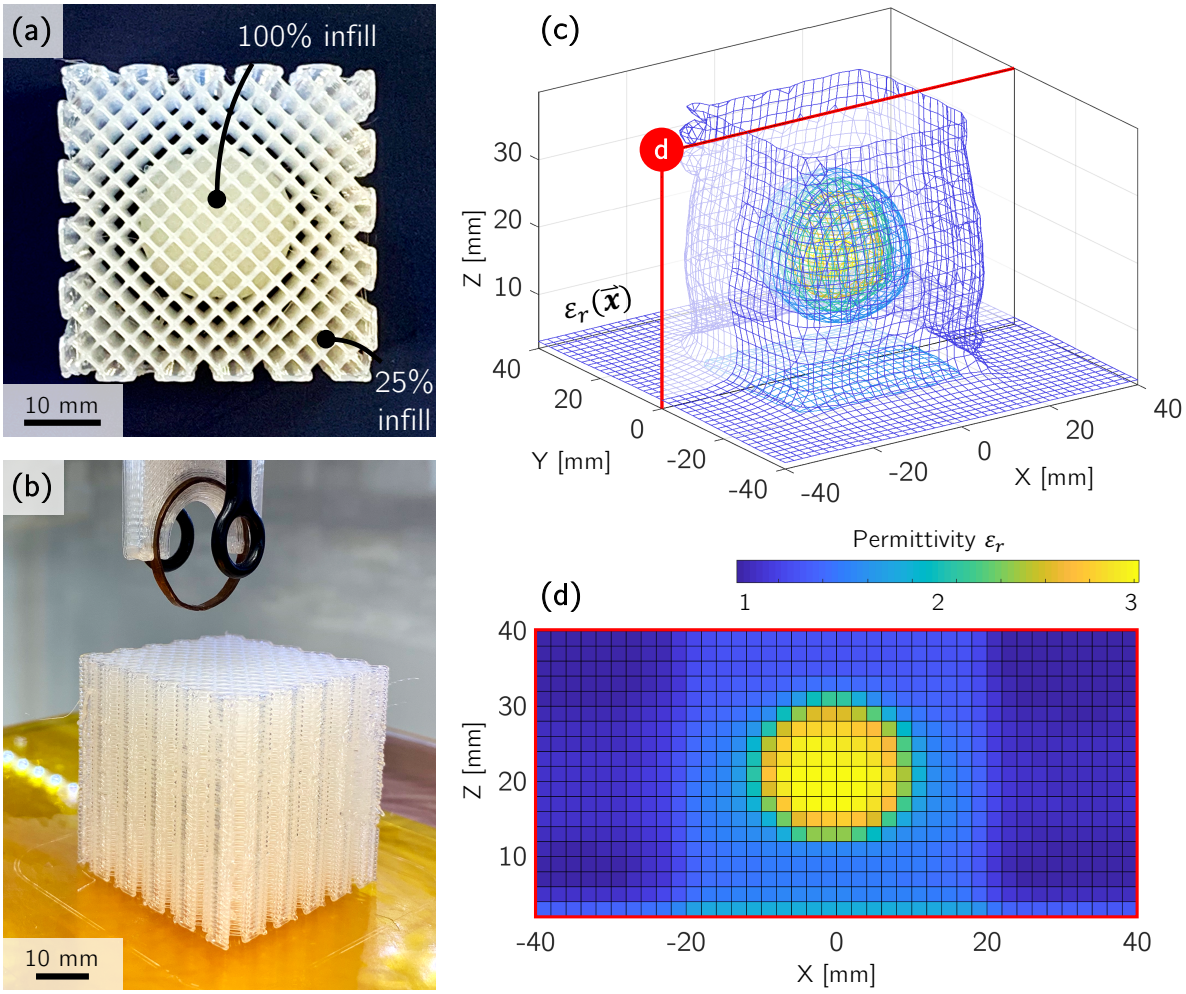

Figure 9: Photographs showing (a) a printed object with varying infill density, and (b) the dielectric imaging module/sensor and object during the later stages of fabrication. Experimental data showing (c) the measured spatial permittivity map $\varepsilon_r(\vec{\mathbf{x}})$ using SRR measurements of f_0 only, and (d) a typical X-Z planar cross-section of $\varepsilon_r(\vec{\mathbf{x}})$.

4. Conclusions and outlook

The *layer-by-layer* nature of AM processes presented an opportunity to integrate a non-destructive, compact surface-based characterization technique *in-line* with device fabrication. Using data obtained during manufacture, it was straightforward to reconstruct 3D images of the spatial distribution of relative dielectric permittivity within a printed part. Data was recorded using a non-contact, sub-wavelength EM characterization technique based on a split ring resonator (SRR). In principle, the real-time assessment of local material properties could provide a near immediate proxy for quality control, at least in terms of the permittivity design. The imaging principle and its limitations have been discussed in detail and proof-of-concept (PoC) experimental data presented.

The methodology shown here could be easily extended to integrate other surface-based techniques *in-line* with AM processes. In particular, the non-contact/non-destructive nature of the dielectric imaging technique may offer opportunities for other AM applications e.g. for monitoring deposition, curing or defects in soft materials, or mapping property changes due to combinations of materials. However, the resolution of the current technique, even after post-processing, was insufficient to detect sub-mm features or small printing defects. Where high spatial resolution is needed, the time penalty from point-by-point scanning over a surface may become significant. For the parameters and apparatus used in this paper, the time to acquire each data point, including the time taken to move in X and Y was approximately 1 s. However, both constraints are likely amenable to further optimization through hardware/software improvement.

This proof-of-concept study has shown that there are some generic challenges related to integrating characterization techiques into AM, and in particular include: (a) the need for open, accessible control software that readily allows for *plug and play* sensor integration and data sampling, (b) a greater range of characterization probes compatible with a wider range of materials and AM processes, and (c) the need for sensor/hardware/software strategies that avoid slow point-by-point scanning of the printed area. Specifically with respect to 3D dielectric imaging using a SRR *in-line* with AM described in this paper, a proof-of-concept demonstration of closed-loop feedback control, i.e. immediately responding to potential (relatively large) printing defects, could now be realistically considered. The investigation of other EM material properties, such as the dielectric loss tangent, may be considered by, for example, relating the quality factor of the resonant transmission signal S_{21} to the loss tangent in an analogous manner to the method described in this

paper for relating f_0 to ε_r. Furthermore, increasing the operating frequency of the SRR system (i.e. using a smaller ring) will lead to improved spatial resolution and may allow the detection of smaller printing defects. The resonant ring dimensions used here were primarily for convenience derived from our prior work on developing the SRR concept [19] and for proof-of-concept, while Appendix B describes how the geometry can easily be varied to explore different frequencies and spatial resolutions.

Acknowledgements

The authors would like to thank the UK Engineering and Physical Sciences Research Council (EPSRC reference: EP/N509711/1) for financial support, Robin Vincent and Gideon Ring for support in constructing the bespoke hybrid additive manufacturing machine (hybrid-AM machine).

Works cited

[1] M. Mani, B. Lane, A. Donmez, S. Feng, S. Moylan, R. Fesperman, Measurement Science Needs for Real-time Control of Additive Manufacturing Powder Bed Fusion Processes, Tech. rep., National Institute of Standards and Technology, Gaithersburg, MD (feb 2015). doi:10.6028/NIST.IR.8036.
URL https://nvlpubs.nist.gov/nistpubs/ir/2015/NIST.IR.8036.pdf

[2] E. Pei, M. Ressin, R. I. Campbell, B. Eynard, J. Xiao, Investigating the impact of additive manufacturing data exchange standards for re-distributed manufacturing, Progress in Additive Manufacturing 4 (3) (2019) 331–344. doi:10.1007/s40964-019-00085-7.
URL https://doi.org/10.1007/s40964-019-00085-7

[3] S. Clijsters, T. Craeghs, S. Buls, K. Kempen, J. P. Kruth, In situ quality control of the selective laser melting process using a high-speed, real-time melt pool monitoring system, International Journal of Advanced Manufacturing Technology 75 (5-8) (2014) 1089–1101. doi:10.1007/s00170-014-6214-8.

[4] T. Craeghs, S. Clijsters, J. P. Kruth, F. Bechmann, M. C. Ebert, Detection of Process Failures in Layerwise Laser Melting with Optical Process Monitoring, Physics Procedia 39 (2012) 753–759. doi:10.1016/j.phpro.2012.10.097.
URL http://dx.doi.org/10.1016/j.phpro.2012.10.097

[5] V. Gunenthiram, P. Peyre, M. Schneider, M. Dal, F. Coste, I. Koutiri, R. Fabbro, Experimental analysis of spatter generation and melt-pool behavior during the powder bed laser beam melting process, Journal of Materials Processing Technology 251 (February 2017) (2018) 376–386. doi:10.1016/j.jmatprotec.2017.08.012.
URL http://dx.doi.org/10.1016/j.jmatprotec.2017.08.012

[6] Y. Zhang, G. S. Hong, D. Ye, K. Zhu, J. Y. Fuh, Extraction and evaluation of melt pool, plume and spatter information for powder-bed fusion AM process monitoring, Materials & Design 156 (2018) 458–469. doi:10.1016/j.matdes.2018.07.002.
URL https://doi.org/10.1016/j.matdes.2018.07.002

[7] Q. Sun, G. Rizvi, C. Bellehumeur, P. Gu, Effect of processing conditions on the bonding quality of FDM polymer filaments, Rapid Prototyping Journal 14 (2) (2008) 72–80. doi:10.1108/13552540810862028.
URL http://www.emeraldinsight.com/doi/10.1108/13552540810862028

[8] M. Hirsch, R. Patel, W. Li, G. Guan, R. K. Leach, S. D. Sharples, A. T. Clare, Assessing the capability of in-situ nondestructive analysis during layer based additive manufacture, Additive Manufacturing 13 (2017) 135–142. doi:10.1016/j.addma.2016.10.004.
URL http://dx.doi.org/10.1016/j.addma.2016.10.004

[9] H. Kim, Y. Lin, T.-L. B. Tseng, A review on quality control in additive manufacturing, Rapid Prototyping Journal 24 (3) (2018) 645–669. arXiv:/doi.org/10.1108/RPJ-03-2017-0048, doi:10.1108/RPJ-03-2017-0048.
URL http://www.emeraldinsight.com/doi/10.1108/RPJ-03-2017-0048

[10] J. Mireles, S. Ridwan, P. A. Morton, A. Hinojos, R. B. Wicker, Analysis and correction of defects within parts fabricated using powder bed fusion technology, Surface Topography: Metrology and Properties 3 (3) (2015) 034002. doi:10.1088/2051-672X/3/3/034002.
URL http://stacks.iop.org/2051-672X/3/i=3/a=034002?key=crossref.490c370d521de90fec67fe4be136c2a7

[11] P. Sitthi-Amorn, J. E. Ramos, Y. Wangy, J. Kwan, J. Lan, W. Wang, W. Matusik, MultiFab, ACM Transactions on Graphics 34 (4) (2015) 129:1–129:11. doi:10.1145/2766962.
URL http://dl.acm.org/citation.cfm?doid=2809654.2766962

[12] P. K. Rao, J. P. Liu, D. Roberson, Z. J. Kong, C. Williams, Online Real-Time Quality Monitoring in Additive Manufacturing Processes Using Heterogeneous Sensors, Journal of Manufacturing Science and Engineering 137 (6) (2015) 061007. doi:10.1115/1.4029823.
URL http://manufacturingscience.asmedigitalcollection.asme.org/article.aspx?doi=10.1115/1.4029823

[13] T. J. Coogan, D. O. Kazmer, In-line rheological monitoring of fused deposition modeling, Journal of Rheology 63 (1) (2019) 141–155. doi:10.1122/1.5054648.
URL http://sor.scitation.org/doi/10.1122/1.5054648

[14] C. Kousiatza, D. Tzetzis, D. Karalekas, In-situ characterization of 3D printed continuous fiber reinforced composites: A methodological study using fiber Bragg grating sensors, Composites Science and Technology 174 (November 2018) (2019) 134–141. doi:10.1016/j.compscitech.2019.02.008.
URL https://doi.org/10.1016/j.compscitech.2019.02.008

[15] A. Thompson, I. Maskery, R. K. Leach, X-ray computed tomography for additive manufacturing: A review, Measurement Science and Technology 27 (7). doi:10.1088/0957-0233/27/7/072001.

[16] Y. Wu, D. Isakov, P. Grant, Fabrication of Composite Filaments with High Dielectric Permittivity for Fused Deposition 3D Printing, Materials 10 (10) (2017) 1218. doi:10.3390/ma10101218.
URL http://www.mdpi.com/1996-1944/10/10/1218

[17] L. D. Sturm, M. I. Albakri, P. A. Tarazaga, C. B. Williams, In situ monitoring of material jetting additive manufacturing process via impedance based measurements, Additive Manufacturing 28 (February) (2019) 456–463. doi:10.1016/j.addma.2019.05.022.
URL https://linkinghub.elsevier.com/retrieve/pii/S2214860419300909

[18] S. K. Everton, M. Hirsch, P. I. Stavroulakis, R. K. Leach, A. T. Clare, Review of in-situ process monitoring and in-situ metrology for metal additive manufacturing, Materials and Design 95 (2016) 431–445. doi:10.1016/j.matdes.2016.01.099.
URL http://dx.doi.org/10.1016/j.matdes.2016.01.099

[19] D. Isakov, C. J. Stevens, F. Castles, P. S. Grant, A Split Ring Resonator Dielectric Probe for Near-Field Dielectric Imaging, Scientific Reports 7 (1) (2017) 1–9. doi:10.1038/s41598-017-02176-3.
URL http://dx.doi.org/10.1038/s41598-017-02176-3

[20] X.-S. Jiang, L.-H. Qi, J. Luo, H. Huang, J.-M. Zhou, Research on accurate droplet generation for micro-droplet deposition manufacture, The International Journal of Advanced Manufacturing Technology 49 (5-8) (2010) 535–541. doi:10.1007/s00170-009-2403-2.
URL http://link.springer.com/10.1007/s00170-009-2403-2

[21] C. Kousiatza, D. Karalekas, In-situ monitoring of strain and temperature distributions during fused deposition modeling process, Materials and Design 97 (2016) 400–406. doi:10.1016/j.matdes.2016.02.099.
URL http://dx.doi.org/10.1016/j.matdes.2016.02.099

[22] T. S. Lumpe, J. Mueller, K. Shea, Tensile properties of multi-material interfaces in 3D printed parts, Materials and Design 162 (2019) 1–9. doi:10.1016/j.matdes.2018.11.024.
URL https://doi.org/10.1016/j.matdes.2018.11.024

[23] A. Boschetto, L. Bottini, Roughness prediction in coupled operations of fused deposition modeling and barrel finishing, Journal of Materials Processing Technology 219 (2015) 181–192. doi:10.1016/j.jmatprotec.2014.12.021.
URL http://dx.doi.org/10.1016/j.jmatprotec.2014.12.021https://linkinghub.elsevier.com/retrieve/pii/S0924013614005172

[24] D. Isakov, C. J. Stevens, F. Castles, P. S. Grant, 3D-Printed High Dielectric Contrast Gradient Index Flat Lens for a Directive Antenna with Reduced Dimensions, Advanced Materials Technologies 1 (6) (2016) 1600072. doi:10.1002/admt.201600072.
URL http://doi.wiley.com/10.1002/admt.201600072

[25] Y. Wu, Additive Manufacturing of Graded and Anisotropic Materials for Applications at Microwave Frequencies, University of Oxford.

[26] U. Leonhardt, Optical Conformal Mapping, Science 312 (2013) 1777–1780. arXiv:arXiv:1308.5367, doi:10.1126/science.1126493.
URL http://doi.wiley.com/10.1002/9781118343371.refs

[27] J. B. Pendry, D. Schurig, D. R. Smith, Controlling electromagnetic fields, Science 312 (5781) (2006) 1780–1782. arXiv:0602092, doi:10.1126/science.1125907.

[28] D. H. Kwon, D. H. Werner, Transformation electromagnetics: An overview of the theory and applications, IEEE

Antennas and Propagation Magazine 52 (1) (2010) 24–46. doi:10.1109/MAP.2010.5466396.

[29] P. Deffenbaugh, K. Church, J. Goldfarb, X. Chen, Fully 3D Printed 2.4 GHz Bluetooth/Wi-Fi Antenna, International Symposium on Microelectronics 2013 (1) (2013) 000914–000920. doi:10.4071/isom-2013-THP53.
URL http://imapsource.org/doi/10.4071/isom-2013-THP53

[30] R. C. Rumpf, J. J. Pazos, J. L. Digaum, S. M. Kuebler, Spatially variant periodic structures in electromagnetics, Philosophical Transactions of the Royal Society A: Mathematical, Physical and Engineering Sciences 373 (2049). doi:10.1098/rsta.2014.0359.

[31] K. Kirschenmann, K. W. Whites, S. M. Woessner, Inkjet printed microwave frequency multilayer antennas, in: 2007 IEEE Antennas and Propagation Society International Symposium, no. 1, IEEE, 2007, pp. 924–927. doi:10.1109/APS.2007.4395646.
URL https://ieeexplore.ieee.org/document/4395646/

[32] M. Afsar, J. Birch, R. Clarke, G. Chantry, The measurement of the properties of materials, Proceedings of the IEEE 74 (1) (1986) 183–199. doi:10.1109/PROC.1986.13432.
URL http://ieeexplore.ieee.org/document/1457700/

[33] J. Baker-Jarvis, M. Janezic, D. Degroot, High-frequency dielectric measurements, IEEE Instrumentation & Measurement Magazine 13 (2) (2010) 24–31. doi:10.1109/MIM.2010.5438334.
URL http://ieeexplore.ieee.org/document/5438334/

[34] G. Brodie, M. V. Jacob, P. Farrell, 6 Techniques for Measuring Dielectric Properties, in: Microwave and Radio-Frequency Technologies in Agriculture, De Gruyter Open, Warsaw, Poland, 2015. doi:10.1515/9783110455403-007.
URL https://www.degruyter.com/view/books/9783110455403/9783110455403-007/9783110455403-007.xml

[35] F. Castles, D. Isakov, A. Lui, Q. Lei, C. E. Dancer, Y. Wang, J. M. Janurudin, S. C. Speller, C. R. Grovenor, P. S. Grant, Microwave dielectric characterisation of 3D-printed BaTiO3/ABS polymer composites, Scientific Reports 6 (March) (2016) 1–8. doi:10.1038/srep22714.
URL http://dx.doi.org/10.1038/srep22714

[36] T. T. Grove, M. F. Masters, R. E. Miers, Determining dielectric constants using a parallel plate capacitor, American Journal of Physics 73 (1) (2005) 52–56. doi:10.1119/1.1794757.
URL http://aapt.scitation.org/doi/10.1119/1.1794757

[37] D. Ghodgaonkar, V. Varadan, V. Varadan, Free-space measurement of complex permittivity and complex permeability of magnetic materials at microwave frequencies, IEEE Transactions on Instrumentation and Measurement 39 (2) (1990) 387–394. doi:10.1109/19.52520.
URL http://ieeexplore.ieee.org/document/52520/

[38] F. Costa, M. Borgese, M. Degiorgi, A. Monorchio, Electromagnetic Characterisation of Materials by Using Transmission/Reflection (T/R) Devices, Electronics 6 (4) (2017) 95. doi:10.3390/electronics6040095.
URL http://www.mdpi.com/2079-9292/6/4/95

[39] T. Athey, M. Stuchly, S. Stuchly, Measurement of Radio Frequency Permittivity of Biological Tissues with an Open-Ended Coaxial Line: Part I, IEEE Transactions on Microwave Theory and Techniques 30 (1) (1982) 82–86. doi:10.1109/TMTT.1982.1131021.

URL http://ieeexplore.ieee.org/document/1131021/

[40] H. Yue, K. L. Virga, J. L. Prince, Dielectric constant and loss tangent measurement using a stripline fixture, IEEE Transactions on Components, Packaging, and Manufacturing Technology: Part B 21 (4) (1998) 441–446. doi:10.1109/96.730430.

URL http://ieeexplore.ieee.org/document/730430/

[41] L. Fieber, J. D. Evans, C. Huang, P. S. Grant, Single-operation, multi-phase additive manufacture of electrochemical double layer capacitor devices, Additive Manufacturing 28 (May) (2019) 344–353. doi:10.1016/j.addma.2019.05.001.

URL https://linkinghub.elsevier.com/retrieve/pii/S2214860419301319

[42] C. Dichtl, P. Sippel, S. Krohns, Dielectric Properties of 3D Printed Polylactic Acid, Advances in Materials Science and Engineering 2017 (2017) 1–10. doi:10.1155/2017/6913835.

URL https://www.hindawi.com/journals/amse/2017/6913835/

[43] A. N. Vicente, G. M. Dip, C. Junqueira, The step by step development of NRW method, in: 2011 SBMO/IEEE MTT-S International Microwave and Optoelectronics Conference (IMOC 2011), IEEE, 2011, pp. 738–742. doi:10.1109/IMOC.2011.6169318.

URL http://ieeexplore.ieee.org/document/6169318/

[44] R. Liu, J. Jia, Reducing boundary artifacts in image deconvolution, Proceedings - International Conference on Image Processing, ICIP (2008) 505–508doi:10.1109/ICIP.2008.4711802.

[45] O. Wiener, Zur theorie der refraktionskonstanten, in: Berichte uber Verhandlungen Koniglich-Sachsischen Gesellschaft Wisseschaften Leipzig, 1910, pp. 256–277.

[46] O. Sydoruk, E. Tatartschuk, E. Shamonina, L. Solymar, Analytical formulation for the resonant frequency of split rings, Journal of Applied Physics 105 (1) (2009) 014903. doi:10.1063/1.3056052.

URL http://aip.scitation.org/doi/10.1063/1.3056052

[47] Azom, Properties of Borosilicate Glass (2019).

URL https://www.azom.com/article.aspx?ArticleID=4765

Appendices

A. Supplementary figures

A.1. Split ring resonator module

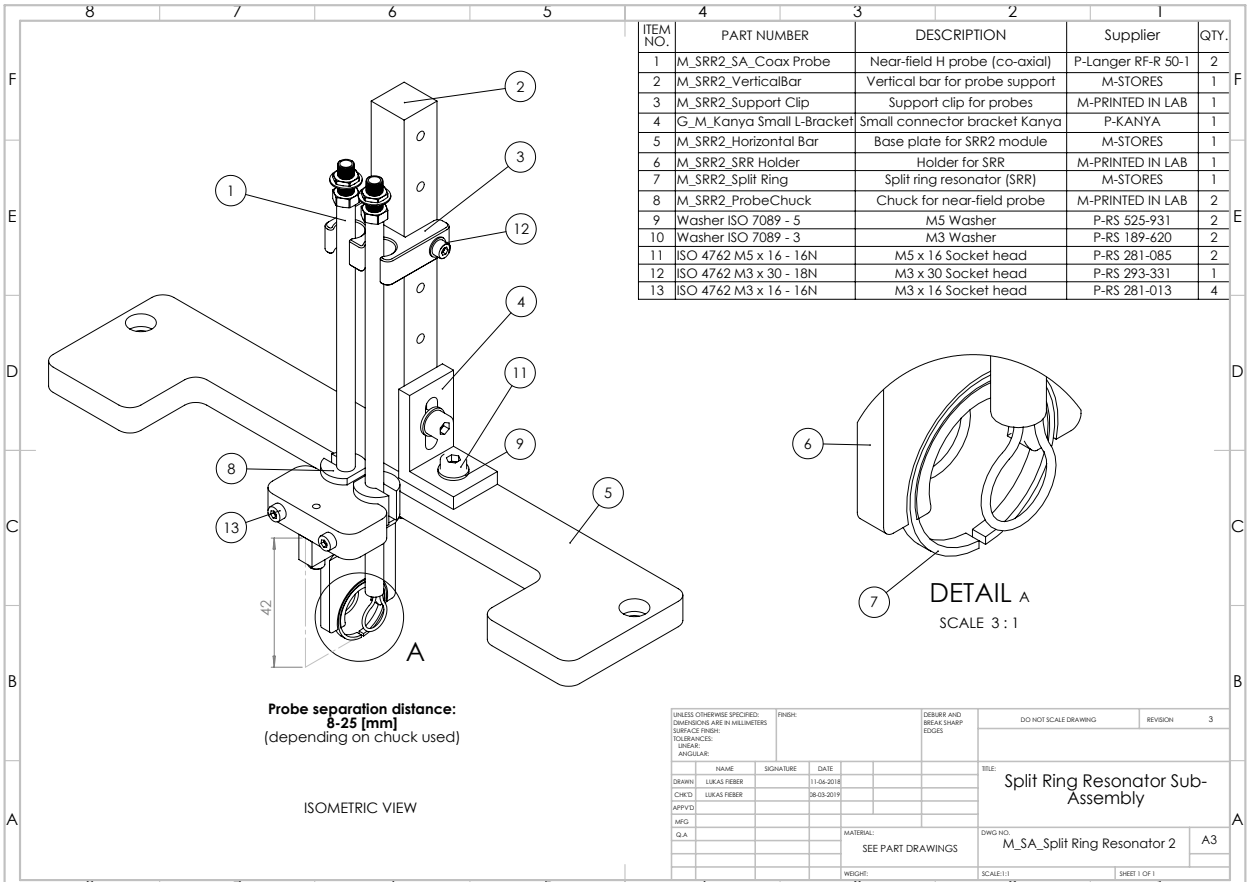

Figure A.1: Engineering drawing of the SRR module sub-assembly.

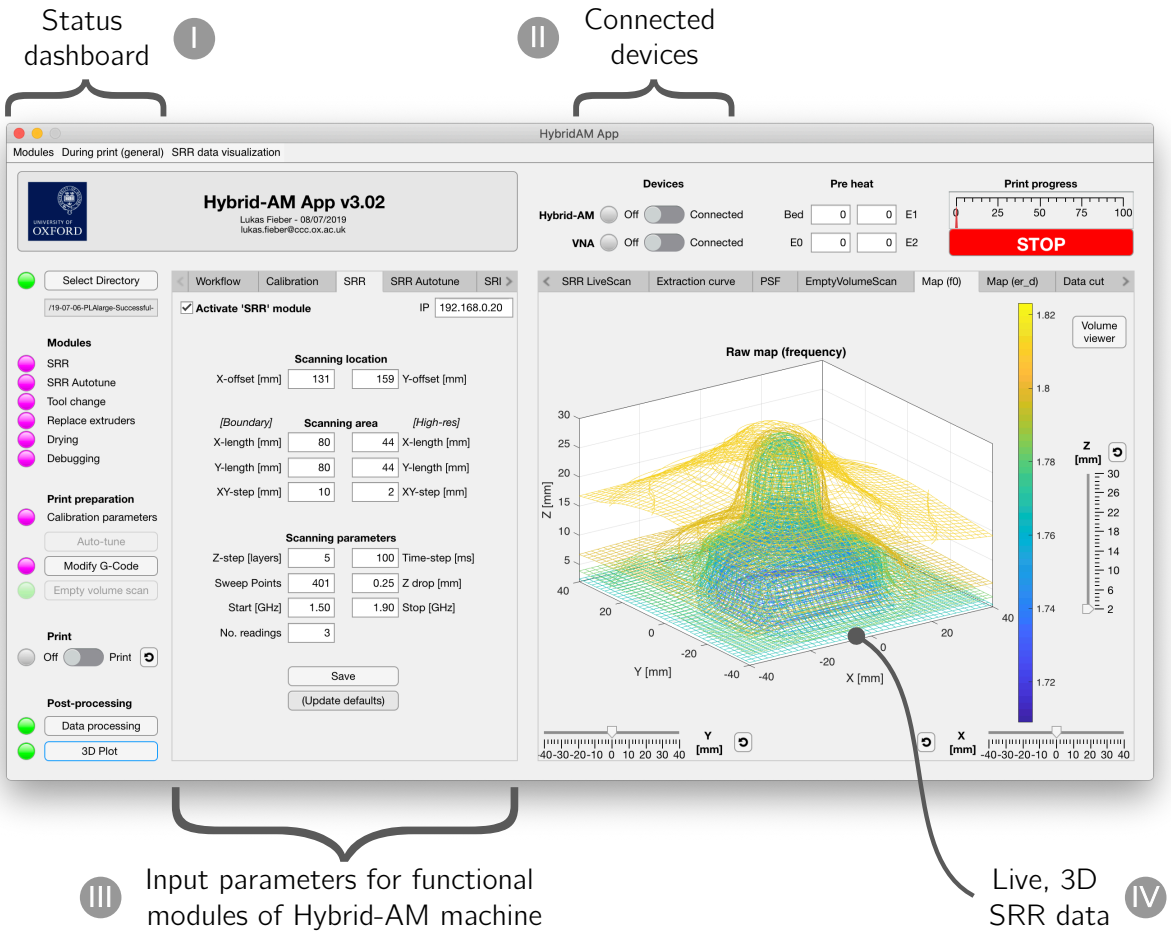

Figure A.2: Screenshot of the GUI for the hybrid-AM app showing (i) the status dashboard and activated functional modules, (ii) connected devices, (iii) module specific tabs for inputting parameters and (iv) live 3D contour plots of the SRR data during print.

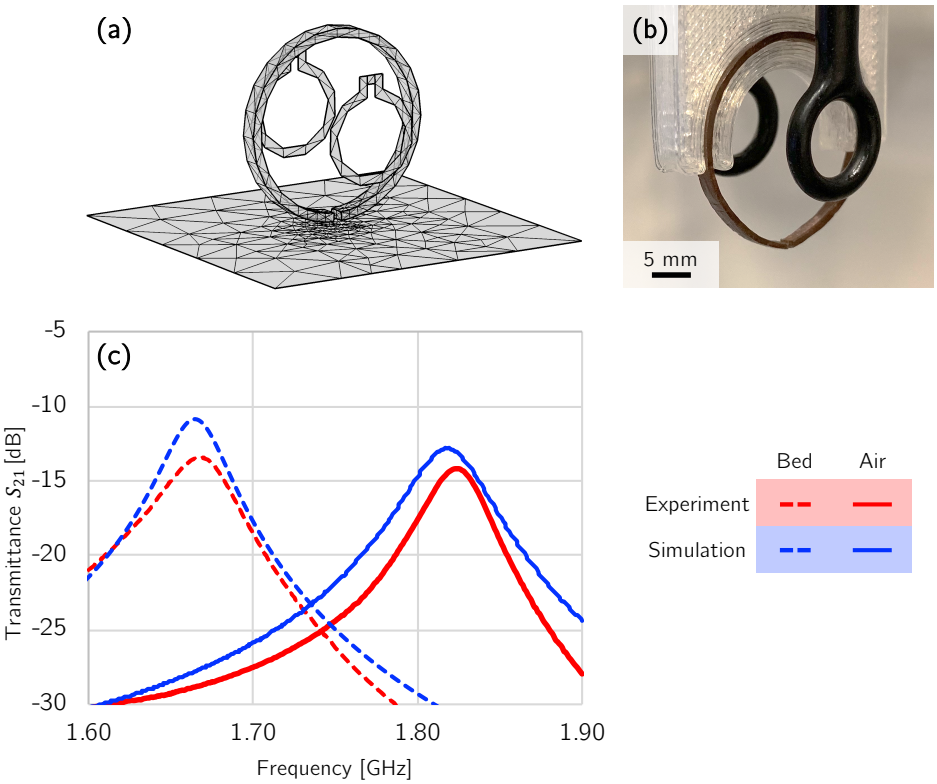

Figure A.3: A comparison of the transmission parameter S_{21} between (a) simulation and (b) experiments for a SRR in free space ($\varepsilon_r = 1$) and in proximity to the build platform ($\varepsilon_r = 5.6$).

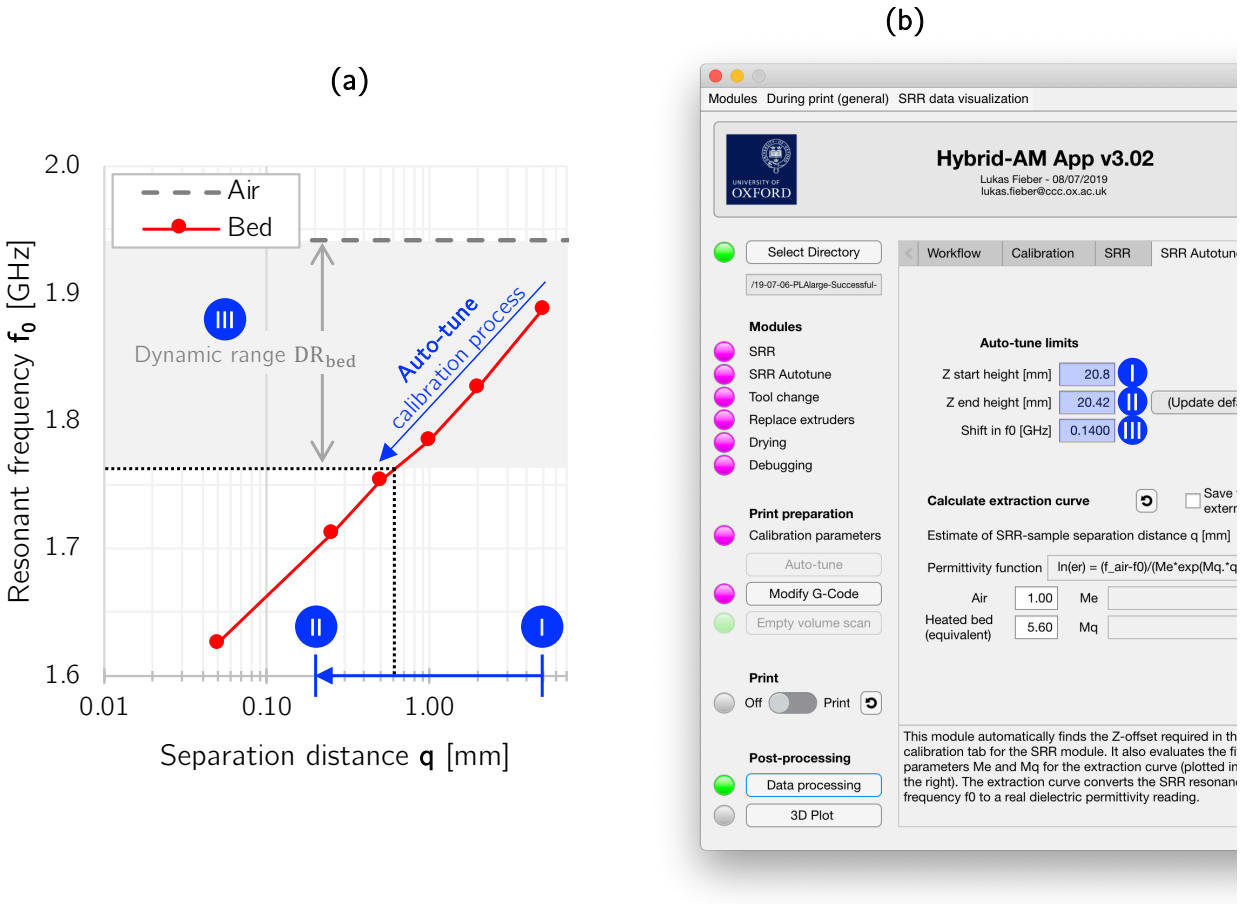

Figure A.4: (a) The influence of probe-bed separation distance q on the SRR resonant frequency and (b) a screenshot of the control software GUI for initiating the automated SRR calibration process.

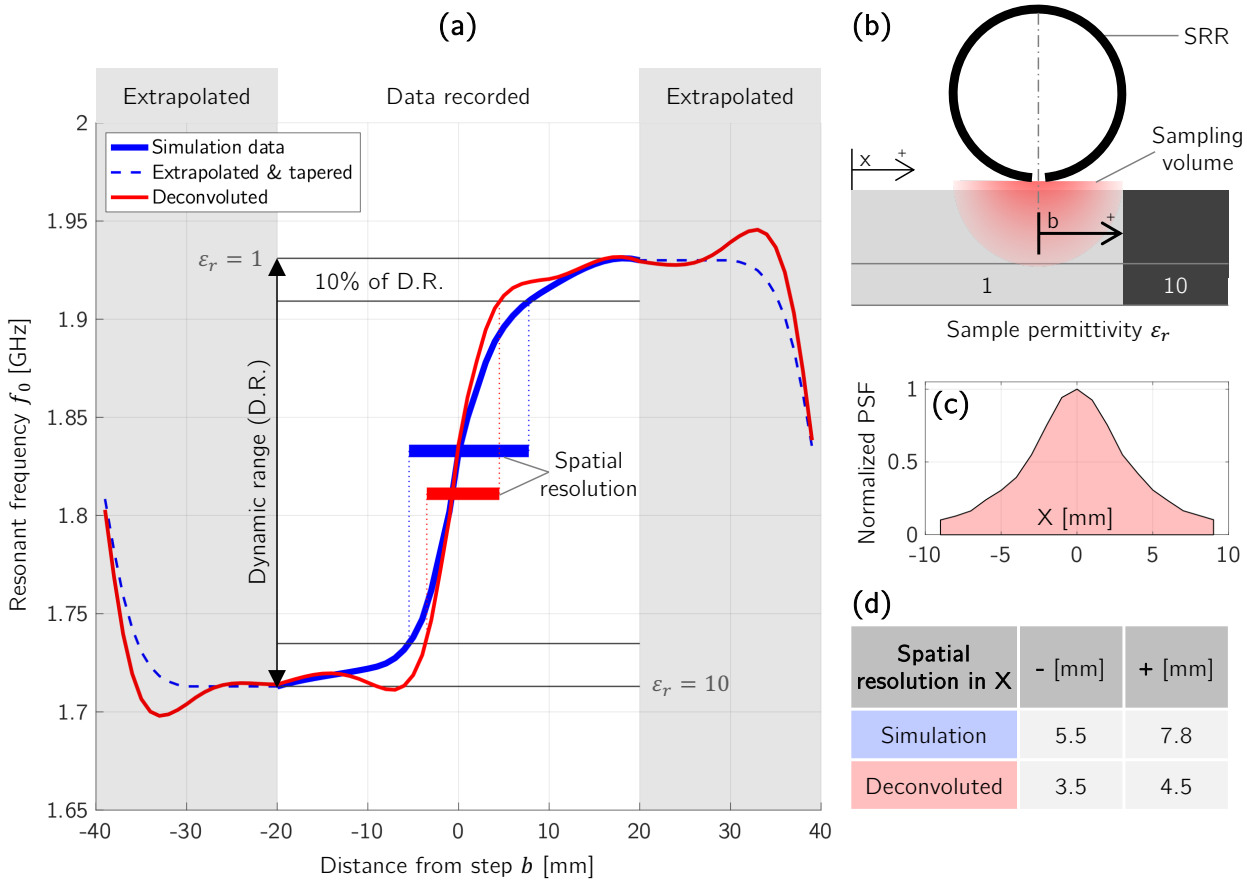

Figure A.5: (a) Simulation data showing the spatial resolution limit of the SRR in the x-axis, (b) a schematic of the experimental setup used for simulation, (c) the PSF used for deconvolution and (d) an indication of the impact deconvolution had on spatial resolution.

B. Geometric factors influencing the intrinsic resonant frequency of a SRR

The intrinsic resonant frequency of the SRR (i.e. f_0 for an ideal, singly split ring resonator in free space with permittivity and permeability ε_0 and μ_0 respectively, excluding any peripheral contributions) may be modelled as an equivalent electronic L-C circuit as expressed in Equation (6). The total capacitance of the resonating system C_{tot} is given by Equation (7): the sum of the parallel plate capacitance C_{gap} (across the air gap), and the capacitance of the SRR surface C_{ring}. The magnetic inductance L as well as C_{gap} and C_{ring} may be expressed analytically from [46], see Equations (8) to (10), as a function of geometric SRR parameters (ring width w, thickness h, internal radius R and air gap g, defined in Figure B.1b). Figure B.1 shows a plot of the analytical equations for geometric parameters comparable to those used for the *in-line* dielectric characterization technique. R_m was defined as the average radius of the SRR ($R_m = R + w/2$).

$$f_{0,air} = \frac{1}{2\pi\sqrt{LC_{tot}}} \tag{6}$$

$$C_{tot} = C_{gap} + C_{ring} \tag{7}$$

$$C_{gap} = \varepsilon_0 \left(\frac{hw}{g}\right) + \varepsilon_0(h + w + g) \tag{8}$$

$$C_{ring} = 2\varepsilon_0 \left[\frac{h + w}{\pi} \ln\left(\frac{4R}{g}\right)\right] \tag{9}$$

$$L = \mu_0 R_m \left[\ln\left(\frac{8R_m}{h + w}\right) - \frac{1}{2}\right] \tag{10}$$

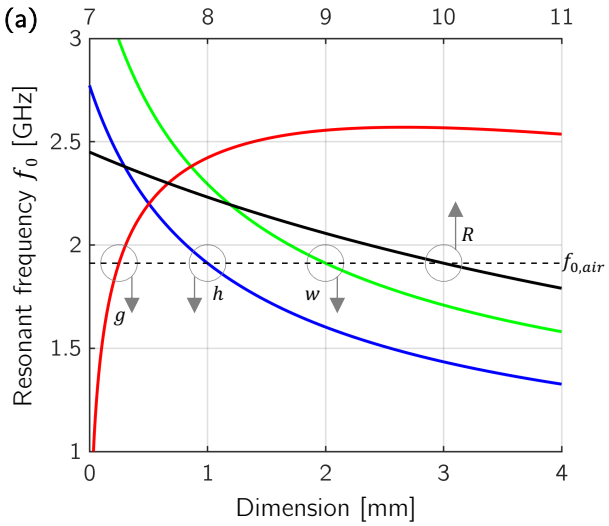

(b*)

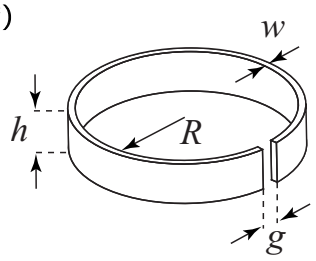

(c)

Dimension			Description
g	0.25	mm	Air gap
h	1	"	Thickness
R	10	"	Internal radius
w	2	"	Width

*Schematic in (b) from Sydoruk et al., 2009

Figure B.1: (a) The intrinsic resonant frequency (f_0) of a SRR in free space as a function of geometric parameters, (b) definition of geometric parameters (schematic from [46]) and (c) default geometric parameters used.

C. Considerations related to the SRR system

The control system (e.g. meshing distribution/density and NC parameters) as well as the calibration of the SRR system (e.g. mechanical offset, perpendicularity to the probe to the print-bed) influenced the quality of 3D SRR measurements (i.e. the *raw* data: $f_{ref}(\vec{\mathbf{x}})$ and $f_0(\vec{\mathbf{x}})$ in Figure 3).

Meshing. A series of time-saving measures, shown in Figure C.1, were implemented in the automated meshing process to speed up the sampling: (a) a *coarse*, 9-point mesh and skipping of sampling layers for the *empty volume scan* $f_{ref}(\vec{\mathbf{x}})$, and (b) a variable mesh density with a high resolution core (where the print part was) and a coarse perimeter. To generate a map with uniform denisty, data points were interpolated using a spline algorithm. Applicable metadata (e.g. the size and location of the printed part) was automatically extracted from the `g-Code`.

Electro-magnetic shield and equivalent bed permittivity. The build platform was comprised of a glass plate (4 mm thick borosilicate glass, ε_r= 4.6 [47]), a heated silicone bed with internal electronics (heaters, sensors, wiring) and mechanical fixtures, (Al bars, insulation material, etc.). Figure C.2a shows that the recorded f_0 was noticably influenced by the silicon bed and fixtures which may be interpreted as unwanted *background noise* ($\sim 25\,\%$ of the dynamic range DR_{bed} for $\varepsilon_r \in [1, 5]$). An EM shield (Cu foil) was inserted between the silicon bed and glass plate to reduce this effect (see Figure C.2b). The introduction of Cu with very high relative dielectric permittivity ($\varepsilon_r \to \infty$) and the influence this had on the reference frequency $f_{0,bed}$ was considered. To simplify the extraction model, the build platform was considered to have an *equivalent* permittivity of ε_r= 5.6 (see Figure C.3).

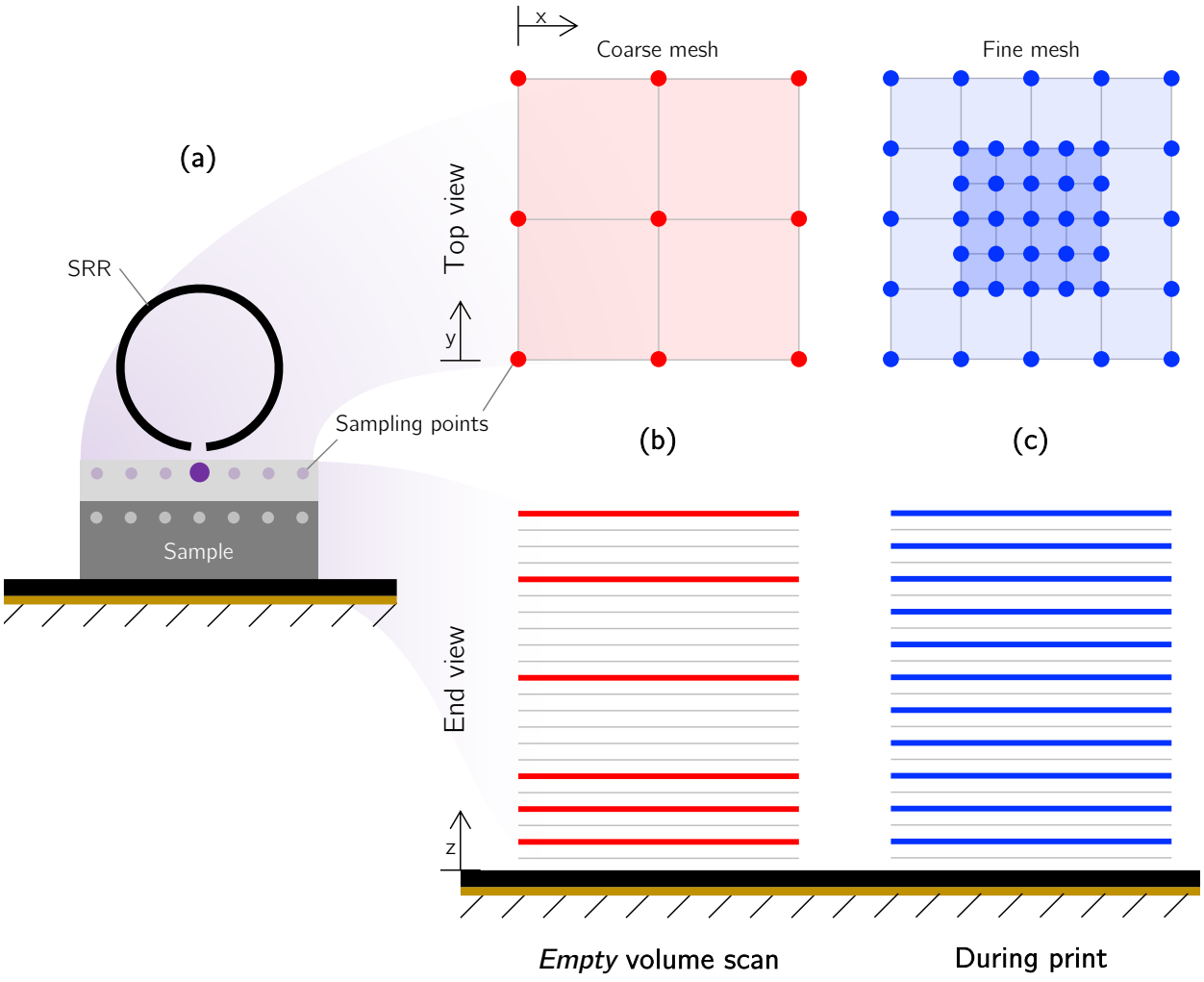

Figure C.1: Schematic illustration of the meshing process.

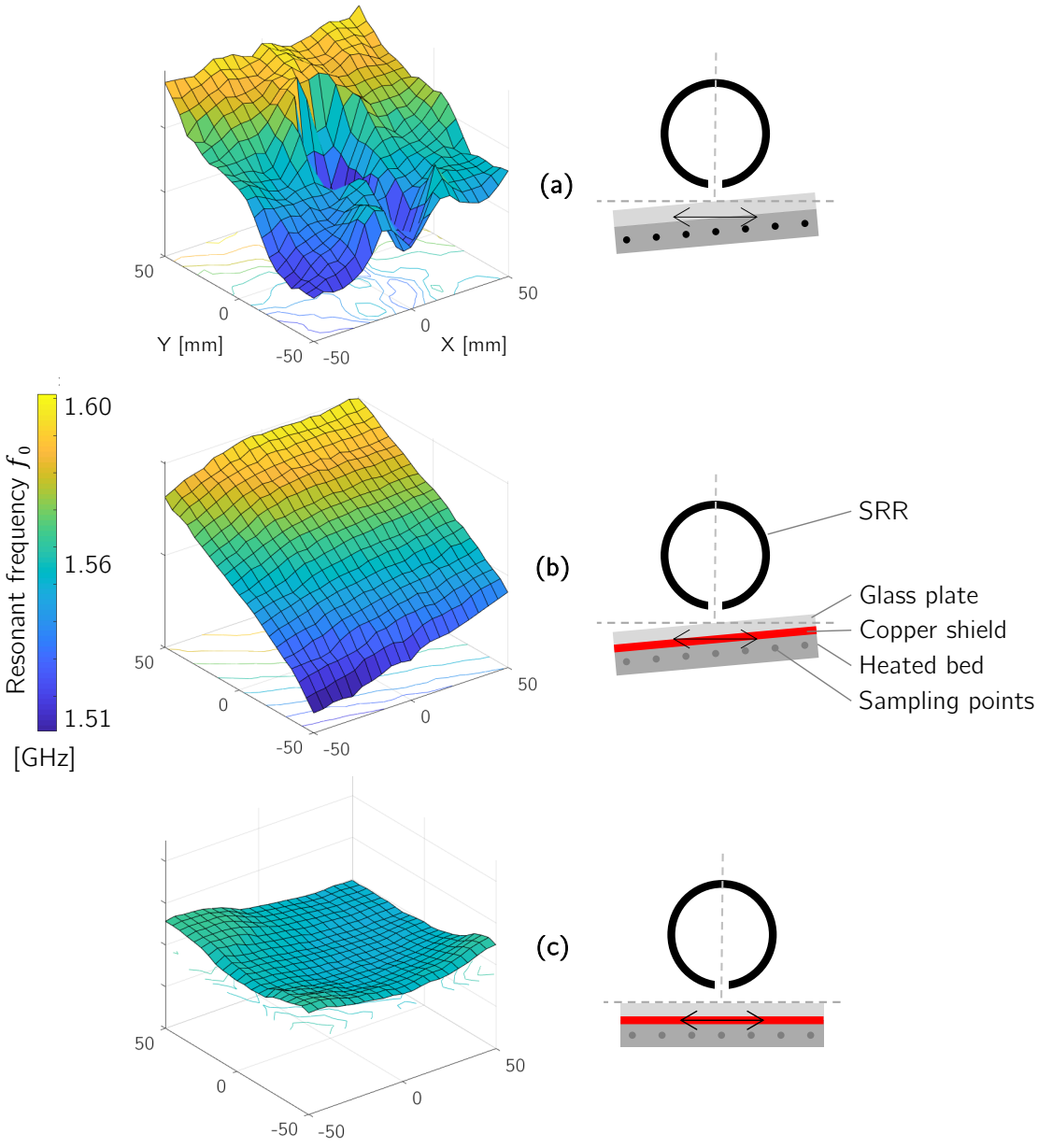

Figure C.2: Experimental data for an XY-scan of SRR resonant frequency f_0 for an empty build-plate showing: (a) build plate, consisting of a glass plate and heated bed, not parallel to build-plate motion, (b) the addition of a copper shield as electric conductor and (c) build plate with copper shield parallel to motion.

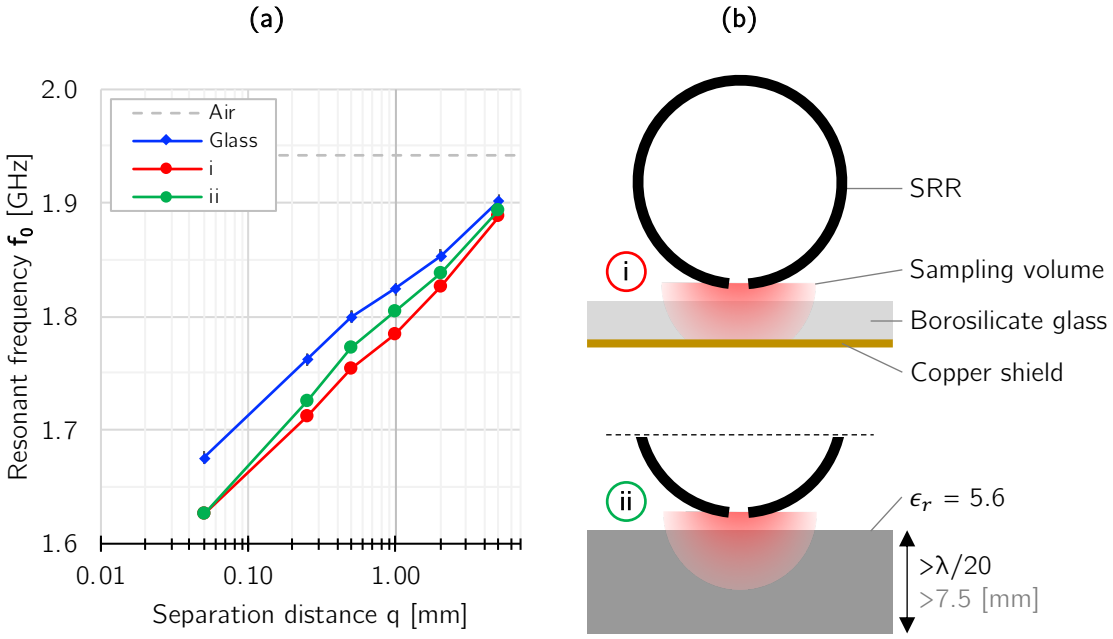

Figure C.3: (a) Simulation data showing the resonant frequency (f_0) as a function of separation distance q for (b) various build-plate configurations: (i) a borosilicate glass plate with a Cu shield and (ii) a simplified build platform of quasi-infinite thickness with an overall equivalent permittivity of $\varepsilon_r = 5.6$.

Works cited

[1] M. Mani, B. Lane, A. Donmez, S. Feng, S. Moylan, R. Fesperman, Measurement Science Needs for Real-time Control of Additive Manufacturing Powder Bed Fusion Processes, Tech. rep., National Institute of Standards and Technology, Gaithersburg, MD (feb 2015). doi:10.6028/NIST.IR.8036.
URL https://nvlpubs.nist.gov/nistpubs/ir/2015/NIST.IR.8036.pdf

[2] E. Pei, M. Ressin, R. I. Campbell, B. Eynard, J. Xiao, Investigating the impact of additive manufacturing data exchange standards for re-distributed manufacturing, Progress in Additive Manufacturing 4 (3) (2019) 331–344. doi:10.1007/s40964-019-00085-7.
URL https://doi.org/10.1007/s40964-019-00085-7

[3] S. Clijsters, T. Craeghs, S. Buls, K. Kempen, J. P. Kruth, In situ quality control of the selective laser melting process using a high-speed, real-time melt pool monitoring system, International Journal of Advanced Manufacturing Technology 75 (5-8) (2014) 1089–1101. doi:10.1007/s00170-014-6214-8.

[4] T. Craeghs, S. Clijsters, J. P. Kruth, F. Bechmann, M. C. Ebert, Detection of Process Failures in Layerwise Laser Melting with Optical Process Monitoring, Physics Procedia 39 (2012) 753–759. doi:10.1016/j.phpro.2012.10.097.
URL http://dx.doi.org/10.1016/j.phpro.2012.10.097

[5] V. Gunenthiram, P. Peyre, M. Schneider, M. Dal, F. Coste, I. Koutiri, R. Fabbro, Experimental analysis of spatter generation and melt-pool behavior during the powder bed laser beam melting process, Journal of Materials Processing Technology 251 (February 2017) (2018) 376–386. doi:10.1016/j.jmatprotec.2017.08.012.
URL http://dx.doi.org/10.1016/j.jmatprotec.2017.08.012

[6] Y. Zhang, G. S. Hong, D. Ye, K. Zhu, J. Y. Fuh, Extraction and evaluation of melt pool, plume and spatter information for powder-bed fusion AM process monitoring, Materials & Design 156 (2018) 458–469. doi:10.1016/j.matdes.2018.07.002.
URL https://doi.org/10.1016/j.matdes.2018.07.002

[7] Q. Sun, G. Rizvi, C. Bellehumeur, P. Gu, Effect of processing conditions on the bonding quality of FDM polymer filaments, Rapid Prototyping Journal 14 (2) (2008) 72–80. doi:10.1108/13552540810862028.
URL http://www.emeraldinsight.com/doi/10.1108/13552540810862028

[8] M. Hirsch, R. Patel, W. Li, G. Guan, R. K. Leach, S. D. Sharples, A. T. Clare, Assessing the capability of in-situ nondestructive analysis during layer based additive manufacture, Additive Manufacturing 13 (2017) 135–142. doi:10.1016/j.addma.2016.10.004.
URL http://dx.doi.org/10.1016/j.addma.2016.10.004

[9] H. Kim, Y. Lin, T.-L. B. Tseng, A review on quality control in additive manufacturing, Rapid Prototyping Journal 24 (3) (2018) 645–669. arXiv:/doi.org/10.1108/RPJ-03-2017-0048, doi:10.1108/RPJ-03-2017-0048.
URL http://www.emeraldinsight.com/doi/10.1108/RPJ-03-2017-0048

[10] J. Mireles, S. Ridwan, P. A. Morton, A. Hinojos, R. B. Wicker, Analysis and correction of defects within parts fabricated using powder bed fusion technology, Surface Topography: Metrology and Properties 3 (3) (2015)

034002. doi:10.1088/2051-672X/3/3/034002.
URL http://stacks.iop.org/2051-672X/3/i=3/a=034002?key=crossref.490c370d521de90fec67fe4be136c2a7

[11] P. Sitthi-Amorn, J. E. Ramos, Y. Wangy, J. Kwan, J. Lan, W. Wang, W. Matusik, MultiFab, ACM Transactions on Graphics 34 (4) (2015) 129:1–129:11. doi:10.1145/2766962.
URL http://dl.acm.org/citation.cfm?doid=2809654.2766962

[12] P. K. Rao, J. P. Liu, D. Roberson, Z. J. Kong, C. Williams, Online Real-Time Quality Monitoring in Additive Manufacturing Processes Using Heterogeneous Sensors, Journal of Manufacturing Science and Engineering 137 (6) (2015) 061007. doi:10.1115/1.4029823.
URL http://manufacturingscience.asmedigitalcollection.asme.org/article.aspx?doi=10.1115/1.4029823

[13] T. J. Coogan, D. O. Kazmer, In-line rheological monitoring of fused deposition modeling, Journal of Rheology 63 (1) (2019) 141–155. doi:10.1122/1.5054648.
URL http://sor.scitation.org/doi/10.1122/1.5054648

[14] C. Kousiatza, D. Tzetzis, D. Karalekas, In-situ characterization of 3D printed continuous fiber reinforced composites: A methodological study using fiber Bragg grating sensors, Composites Science and Technology 174 (November 2018) (2019) 134–141. doi:10.1016/j.compscitech.2019.02.008.
URL https://doi.org/10.1016/j.compscitech.2019.02.008

[15] A. Thompson, I. Maskery, R. K. Leach, X-ray computed tomography for additive manufacturing: A review, Measurement Science and Technology 27 (7). doi:10.1088/0957-0233/27/7/072001.

[16] Y. Wu, D. Isakov, P. Grant, Fabrication of Composite Filaments with High Dielectric Permittivity for Fused Deposition 3D Printing, Materials 10 (10) (2017) 1218. doi:10.3390/ma10101218.
URL http://www.mdpi.com/1996-1944/10/10/1218

[17] L. D. Sturm, M. I. Albakri, P. A. Tarazaga, C. B. Williams, In situ monitoring of material jetting additive manufacturing process via impedance based measurements, Additive Manufacturing 28 (February) (2019) 456–463. doi:10.1016/j.addma.2019.05.022.
URL https://linkinghub.elsevier.com/retrieve/pii/S2214860419300909

[18] S. K. Everton, M. Hirsch, P. I. Stavroulakis, R. K. Leach, A. T. Clare, Review of in-situ process monitoring and in-situ metrology for metal additive manufacturing, Materials and Design 95 (2016) 431–445. doi:10.1016/j.matdes.2016.01.099.
URL http://dx.doi.org/10.1016/j.matdes.2016.01.099

[19] D. Isakov, C. J. Stevens, F. Castles, P. S. Grant, A Split Ring Resonator Dielectric Probe for Near-Field Dielectric Imaging, Scientific Reports 7 (1) (2017) 1–9. doi:10.1038/s41598-017-02176-3.
URL http://dx.doi.org/10.1038/s41598-017-02176-3

[20] X.-S. Jiang, L.-H. Qi, J. Luo, H. Huang, J.-M. Zhou, Research on accurate droplet generation for micro-droplet deposition manufacture, The International Journal of Advanced Manufacturing Technology 49 (5-8) (2010) 535–541. doi:10.1007/s00170-009-2403-2.
URL http://link.springer.com/10.1007/s00170-009-2403-2

[21] C. Kousiatza, D. Karalekas, In-situ monitoring of strain and temperature distributions during fused deposition

modeling process, Materials and Design 97 (2016) 400–406. doi:10.1016/j.matdes.2016.02.099.
URL http://dx.doi.org/10.1016/j.matdes.2016.02.099

[22] T. S. Lumpe, J. Mueller, K. Shea, Tensile properties of multi-material interfaces in 3D printed parts, Materials and Design 162 (2019) 1–9. doi:10.1016/j.matdes.2018.11.024.
URL https://doi.org/10.1016/j.matdes.2018.11.024

[23] A. Boschetto, L. Bottini, Roughness prediction in coupled operations of fused deposition modeling and barrel finishing, Journal of Materials Processing Technology 219 (2015) 181–192. doi:10.1016/j.jmatprotec.2014.12.021.
URL http://dx.doi.org/10.1016/j.jmatprotec.2014.12.021https://linkinghub.elsevier.com/retrieve/pii/S0924013614005172

[24] D. Isakov, C. J. Stevens, F. Castles, P. S. Grant, 3D-Printed High Dielectric Contrast Gradient Index Flat Lens for a Directive Antenna with Reduced Dimensions, Advanced Materials Technologies 1 (6) (2016) 1600072. doi:10.1002/admt.201600072.
URL http://doi.wiley.com/10.1002/admt.201600072

[25] Y. Wu, Additive Manufacturing of Graded and Anisotropic Materials for Applications at Microwave Frequencies, University of Oxford.

[26] U. Leonhardt, Optical Conformal Mapping, Science 312 (2013) 1777–1780. arXiv:arXiv:1308.5367, doi:10.1126/science.1126493.
URL http://doi.wiley.com/10.1002/9781118343371.refs

[27] J. B. Pendry, D. Schurig, D. R. Smith, Controlling electromagnetic fields, Science 312 (5781) (2006) 1780–1782. arXiv:0602092, doi:10.1126/science.1125907.

[28] D. H. Kwon, D. H. Werner, Transformation electromagnetics: An overview of the theory and applications, IEEE Antennas and Propagation Magazine 52 (1) (2010) 24–46. doi:10.1109/MAP.2010.5466396.

[29] P. Deffenbaugh, K. Church, J. Goldfarb, X. Chen, Fully 3D Printed 2.4 GHz Bluetooth/Wi-Fi Antenna, International Symposium on Microelectronics 2013 (1) (2013) 000914–000920. doi:10.4071/isom-2013-THP53.
URL http://imapsource.org/doi/10.4071/isom-2013-THP53

[30] R. C. Rumpf, J. J. Pazos, J. L. Digaum, S. M. Kuebler, Spatially variant periodic structures in electromagnetics, Philosophical Transactions of the Royal Society A: Mathematical, Physical and Engineering Sciences 373 (2049). doi:10.1098/rsta.2014.0359.

[31] K. Kirschenmann, K. W. Whites, S. M. Woessner, Inkjet printed microwave frequency multilayer antennas, in: 2007 IEEE Antennas and Propagation Society International Symposium, no. 1, IEEE, 2007, pp. 924–927. doi:10.1109/APS.2007.4395646.
URL https://ieeexplore.ieee.org/document/4395646/

[32] M. Afsar, J. Birch, R. Clarke, G. Chantry, The measurement of the properties of materials, Proceedings of the IEEE 74 (1) (1986) 183–199. doi:10.1109/PROC.1986.13432.
URL http://ieeexplore.ieee.org/document/1457700/

[33] J. Baker-Jarvis, M. Janezic, D. Degroot, High-frequency dielectric measurements, IEEE Instrumentation & Measurement Magazine 13 (2) (2010) 24–31. doi:10.1109/MIM.2010.5438334.

URL http://ieeexplore.ieee.org/document/5438334/

[34] G. Brodie, M. V. Jacob, P. Farrell, 6 Techniques for Measuring Dielectric Properties, in: Microwave and Radio-Frequency Technologies in Agriculture, De Gruyter Open, Warsaw, Poland, 2015. doi:10.1515/9783110455403-007.

URL https://www.degruyter.com/view/books/9783110455403/9783110455403-007/9783110455403-007.xml

[35] F. Castles, D. Isakov, A. Lui, Q. Lei, C. E. Dancer, Y. Wang, J. M. Janurudin, S. C. Speller, C. R. Grovenor, P. S. Grant, Microwave dielectric characterisation of 3D-printed BaTiO3/ABS polymer composites, Scientific Reports 6 (March) (2016) 1–8. doi:10.1038/srep22714.

URL http://dx.doi.org/10.1038/srep22714

[36] T. T. Grove, M. F. Masters, R. E. Miers, Determining dielectric constants using a parallel plate capacitor, American Journal of Physics 73 (1) (2005) 52–56. doi:10.1119/1.1794757.

URL http://aapt.scitation.org/doi/10.1119/1.1794757

[37] D. Ghodgaonkar, V. Varadan, V. Varadan, Free-space measurement of complex permittivity and complex permeability of magnetic materials at microwave frequencies, IEEE Transactions on Instrumentation and Measurement 39 (2) (1990) 387–394. doi:10.1109/19.52520.

URL http://ieeexplore.ieee.org/document/52520/

[38] F. Costa, M. Borgese, M. Degiorgi, A. Monorchio, Electromagnetic Characterisation of Materials by Using Transmission/Reflection (T/R) Devices, Electronics 6 (4) (2017) 95. doi:10.3390/electronics6040095.

URL http://www.mdpi.com/2079-9292/6/4/95

[39] T. Athey, M. Stuchly, S. Stuchly, Measurement of Radio Frequency Permittivity of Biological Tissues with an Open-Ended Coaxial Line: Part I, IEEE Transactions on Microwave Theory and Techniques 30 (1) (1982) 82–86. doi:10.1109/TMTT.1982.1131021.

URL http://ieeexplore.ieee.org/document/1131021/

[40] H. Yue, K. L. Virga, J. L. Prince, Dielectric constant and loss tangent measurement using a stripline fixture, IEEE Transactions on Components, Packaging, and Manufacturing Technology: Part B 21 (4) (1998) 441–446. doi:10.1109/96.730430.

URL http://ieeexplore.ieee.org/document/730430/

[41] L. Fieber, J. D. Evans, C. Huang, P. S. Grant, Single-operation, multi-phase additive manufacture of electrochemical double layer capacitor devices, Additive Manufacturing 28 (May) (2019) 344–353. doi:10.1016/j.addma.2019.05.001.

URL https://linkinghub.elsevier.com/retrieve/pii/S2214860419301319

[42] C. Dichtl, P. Sippel, S. Krohns, Dielectric Properties of 3D Printed Polylactic Acid, Advances in Materials Science and Engineering 2017 (2017) 1–10. doi:10.1155/2017/6913835.

URL https://www.hindawi.com/journals/amse/2017/6913835/

[43] A. N. Vicente, G. M. Dip, C. Junqueira, The step by step development of NRW method, in: 2011 SBMO/IEEE MTT-S International Microwave and Optoelectronics Conference (IMOC 2011), IEEE, 2011, pp. 738–742. doi:10.1109/IMOC.2011.6169318.

URL http://ieeexplore.ieee.org/document/6169318/

[44] R. Liu, J. Jia, Reducing boundary artifacts in image deconvolution, Proceedings - International Conference on Image Processing, ICIP (2008) 505–508doi:10.1109/ICIP.2008.4711802.

[45] O. Wiener, Zur theorie der refraktionskonstanten, in: Berichte uber Verhandlungen Koniglich-Sachsischen Gesellschaft Wisseschaften Leipzig, 1910, pp. 256–277.

[46] O. Sydoruk, E. Tatartschuk, E. Shamonina, L. Solymar, Analytical formulation for the resonant frequency of split rings, Journal of Applied Physics 105 (1) (2009) 014903. doi:10.1063/1.3056052.
URL http://aip.scitation.org/doi/10.1063/1.3056052

[47] Azom, Properties of Borosilicate Glass (2019).
URL https://www.azom.com/article.aspx?ArticleID=4765